ACS APPLIED MATERIALS & INTERFACES

www.acsami.org Research Article

# Chitosan-*g*-estrone Nanoparticles of Palbociclib Vanished Hypoxic Breast Tumor after Targeted Delivery: Development and Ultrasound/Photoacoustic Imaging

Abhishesh Kumar Mehata, Virendra Singh, Vikas, Nitesh Singh, Abhijit Mandal, Debabrata Dash, Biplob Koch, and Madaswamy S. Muthu*

Cite This: https://doi.org/10.1021/acsami.3c03184 Read Online

ACCESS | Metrics & More | Article Recommendations | Supporting Information

**ABSTRACT:** Breast cancer is the leading cause of death among women globally. Approximately 80% of all breast cancers diagnosed are overexpressed with estrogen receptors (ERs). In this study, we have developed an estrone (Egen)-grafted chitosan-based polymeric nanocarrier for the targeted delivery of palbociclib (PLB) to breast cancer. The nanoparticles (NPs) were prepared by solvent evaporation using the ionic gelation method and characterized for particle size, zeta potential, polydispersity, surface morphology, surface chemistry, drug entrapment efficiency, cytotoxicity assay, cellular uptake, and apoptosis study. The developed PLB-CS NPs and PLB-CS-g-Egen NPs had a particle size of 116.3 ± 1.53 and 141.6 ± 1.97 nm, respectively. The zeta potential of PLB-CS NPs and PLB-CS-g-Egen NPs was found to be 18.70 ± 0.416 and 12.45 ± 0.574 mV, respectively. The morphological analysis demonstrated that all NPs were spherical in shape and had a smooth surface. An *in vitro* cytotoxicity assay was performed in estrogen receptor (ER)-expressing MCF7 cells and T47D cells, which suggested that targeted NPs were 57.34- and 30.32-fold more cytotoxic compared to the pure PLB, respectively. Additionally, cell cycle analysis confirmed that cell cycle progression from the G1 into S phase was blocked more efficiently by targeted NPs compared to nontargeted NPs and PLB in MCF7 cells. *In vivo* pharmacokinetic studies demonstrated that entrapment of the PLB in the NPs improved the half-life and bioavailability by ~2−3-fold. Further, ultrasound and photoacoustic imaging of DMBA induced breast cancer in the Sprague-Dawley (SD) rat showed that targeted NPs completely vanished breast tumor, reduced hypoxic tumor volume, and suppressed tumor angiogenesis more efficiently compared to the nontargeted NPs and free PLB. Further, *in vitro* hemocompatibility and histopathology studies suggested that NPs were biocompatible and safe for clinical use.

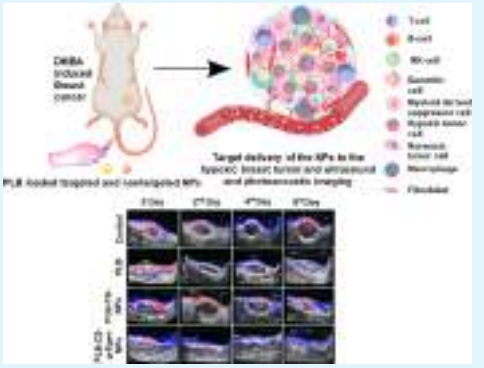

**KEYWORDS:** *breast tumor, estrogen receptor targeted drug delivery, in vivo imaging, palbociclib, ultrasound and photoacoustic imaging*

## INTRODUCTION

Breast cancer is the most common type of cancer in women in the United States and the second leading cause of death among women. About 250,000 new cases of breast cancer are reported in the United States each year.[1] Breast tumor affects one in every 20 women globally and up to one in every eight women in high-income countries, which continues to be the most common cancer-related complication for women.[2] There are important biomarkers that are overexpressed in breast cancers, which include the estrogen receptor (ER), progesterone receptor (PR), and human epidermal growth factor receptor 2 (HER2). Broadly, on the basis of the receptor expressions, breast cancer is categorized into triple-positive breast cancer (ER, PR, and HER2 are overexpressed) and triple-negative breast cancer (devoid of all three receptors). It has been reported that around 83% of breast cancer patients are hormonal receptor (ER+/PR+) positive and responsive toward hormonal treatment for preventing the proliferation of the breast tumor cells.[3,4] Additionally, it has been reported that ~80% of breast cancers diagnosed are ER+.[5] ERs are widely distributed and overexpressed in breast cancers. Generally, ERs are located on the plasma membrane (mER) and nuclear (ER$\alpha$ and ER$\beta$) segment of the breast cancer cells. The expression of the ER in normal breast cells is below 10%, but in cancer cells, overexpression exceeds 80%.[6]

The existing treatment strategy for tumors includes chemotherapy, which causes the cancer cells to shrink, accompanied by surgical resection of the tumor cells. Hormone therapy, radiation therapy, and other cutting-edge techniques

Received: March 5, 2023
Accepted: June 27, 2023




https://doi.org/10.1021/acsami.3c03184
ACS Appl. Mater. Interfaces XXXX, XXX, XXX−XXX

like immunotherapy, photothermal therapy, and genomic therapy are then utilized to prevent the reoccurrence of tumor in the future.[7] As a result, it is crucial to design a combinational therapeutic system using two or more approaches to eliminate their drawbacks and provide a synergistic result.[8−10] Regrettably, chemotherapy has a variety of severe side effects, including neurotoxicity and hypersensitivity. This is mainly because chemotherapy is nonspecific and harms both normal body cells and malignant cells.[11,12] Additionally, the aqueous solubility of several anticancer medicines is limited. Several multipurpose therapeutic systems have been developed to increase anticancer effectiveness while minimizing the adverse effects of chemotherapeutic drugs on normal tissues.[13] Because of the enhanced permeability and retention (EPR) effect, nanoparticle drug delivery technologies in particularly can result in the preferential deposition of medicines inside solid tumors.[14] Estrone (Egen) is a type of estrogen that specifically binds with the ER and has been utilized for the development of the targeted drug delivery system for ER+ breast cancers.[15] In a study, Kurmi *et al.* developed Egen conjugated chitosan (CS) and doxorubicin as dual cancer targeted nanoparticles (NPs) for anticancer activity in MCF7 cells. Enhancement in the cellular cytotoxicity of doxorubicin loaded NPs compared to free doxorubicin was observed in MCF7 cells due to the functionalization of Egen.[16] In another study, Tang *et al.* developed Egen functionalized PEGylated liposomes for the co-delivery of epirubicin and paclitaxel to ER overexpressed breast cancers. Higher cellular uptake and increased tumor accumulation of the targeted NPs were achieved in the MCF7 cells and MCF7 derived tumor bearing mouse model, respectively, due to the functionalization of Egen. Additionally, targeted NPs were able to produce significant tumor suppression properties without producing any toxic effects.[17]

Palbociclib (PLB) is a chemotherapeutic agent developed by Pfizer that inhibits the cyclin-dependent kinases CDK4 and CDK6 in the treatment of advanced breast cancer.[18] The common side effects associated with PLB includes neutropenia, leukopenia, anemia, and fatigue. Additionally, PLB has been found to produce toxicity to the vital organs such as the lungs,[19] liver,[20] and reproductive organs[21] and in the fetus, which is mainly associated with the off-target delivery of PLB. Further, the development of resistance by tumor cells toward the chemotherapeutic agents is very common because of the P-gp efflux pump that effluxes the anticancer drug out of the cancer cells.[22] Researchers have developed an interest in nanotechnology-based cancer therapy strategies due to the enhancement in drug solubility and bioavailability, decrease in toxicity in normal cells, and great promise for tailoring the delivery of drugs to specified parts of the body.[23,24] Polymeric NPs, solid lipid NPs, micelles, and silica NPs are a few examples of the various nanomedicines that have been developed to effectively deliver drugs to advanced mammary carcinomas. These approaches have the potential to be the next generation of drug delivery to combat resistant and metastatic cancerous cells.[25,26] Recently, Kommineni *et al.* designed PLB loaded stealth liposomes for improving the pharmacokinetic profile and anticancer activity in triple-negative 4T1 breast cancer cells. The liposomal system was 1.63-fold more cytotoxic and had 1.45-fold increased $AUC_{tot}$ relative to free PLB.[27] Moreover, Huang *et al.* developed a dimeric prodrug of the PLB linked with a thioketal bond (reactive oxygen species responsive) and co-loaded with Ce6 for combined chemo-photodynamic therapy of triple-negative breast cancers.[28] Apart from these, tumor hypoxia has displayed a key role in breast cancer therapy. Hypoxic breast tumors are highly aggressive, prone to metastasis, and resistant to anticancer drug treatment.[29] Hypoxia arises in tumors because of the rapid proliferation of the tumor cells and poor vascularization, which leads to the distancing of the cells from the nearest source of oxygen.[30] It has been reported that hypoxic tumors are three times more resistant to therapy compared with normoxic tumors.[31] Additionally, the limited vascularization in the hypoxic tumor acts as a barrier to the tumor permeability of the anticancer drug.[32]

Therefore, considering the therapeutic requirement for treating advanced-stage breast cancers, a targeted drug delivery system may be a solution that allows the targeted delivery of the loaded drug to tumors. So, here we proposed ER targeted NPs loaded with PLB for the targeted therapy of advanced-stage breast cancers. First, acid functionalized estrone (Egen-COOH) was covalently conjugated with a CS free amino group (i.e., chitosan-*g*-estrone). Second, PLB was loaded into the CS NPs with the surface assembly of the estrone by modified solvent evaporation with the ionic gelation method. The NPs were characterized for particle size, zeta potential, polydispersity, surface morphology, surface chemistry, drug entrapment efficiency, *in vitro* drug release, X-ray diffraction study, hemolysis, hemocompatibility study, cytotoxicity assay, cellular uptake, apoptosis study, and cell cycle analysis. Coumarin 6 (CM6) loaded NPs were studied for qualitative cellular uptake in the ER overexpressed breast cancer cell lines (i.e., MCF7 and T47D cells). Further, in the *in vitro* cytotoxicity assay of PLB, nontargeted and targeted NPs were evaluated in the MCF7 and T47D cells to calculate $IC_{50}$ values, which indicate the concentration of the drug required to kill 50% of the cancer cells after 24 h of incubation with the formulation. Additionally, pharmacokinetic study and vital organ (brain, lungs, liver, kidney, and spleen) histopathology study were performed in healthy rats for the purpose of assessing pharmacokinetic parameters and any toxicity to the vital organs due to formulation treatments. Moreover, the antitumor activity of the NPs was evaluated in DMBA induced hypoxic breast cancer SD rats, and simultaneous imaging of the breast cancer was performed by ultrasound and a photoacoustic imaging system.

## MATERIALS AND METHODS

**Materials.** Palbociclib was provided by Sun Pharmaceutical Industries Ltd. (Gurugram, India) as a gift sample. Chitosan (CS) (molecular weight ∼1.5 kDa, degree of deacetylation ≥90%), estrone (Egen), succinic anhydride (SA), Na-tripolyphosphate, 4-dimethylaminopyridine (DMAP), *N*-hydroxysuccinimide (NHS), triethylamine (TEA), and *N*-(3-dimethylaminopropyl)-*N*-ethylcarbodiimide (EDC) were supplied by Sisco Research Laboratories Pvt. Ltd. (SRL, India). The human breast cell lines MCF7 and T47D were procured from NCCS Pune, India. Dulbecco's modified Eagle medium (DMEM), fetal bovine serum (FBS), trypsin−EDTA, penicillin−streptomycin solutions, and 12-well cell culture plates were purchased from Cell Clone (Genetix Biotech Asia Pvt. Ltd.). The T-25 cell culture flask and 96-well plates were obtained from Eppendorf. 1,1′-Dioctadecyl-3,3,3′,3′-tetramethylindodicarbocyanine, 4-chlorobenzenesulfonate salt (DiD dye) was purchased from Thermo Fisher Scientific, India. The remaining chemicals used in the experiment were of analytical grade.


https://doi.org/10.1021/acsami.3c03184
ACS Appl. Mater. Interfaces XXXX, XXX, XXX−XXX

## METHODS

**Synthesis of the Chitosan-*g*-estrone (CS-*g*-Egen) Conjugate.** *Activation of Egen-COOH.* The carboxylic acid group was functionalized to Egen by a ring opening polymerization reaction in the presence of SA and DMAP.[33] Egen (1000 mg, 3.7 mmol), TEA (112 mg, 11.12 mmol), and DMAP (46 mg, 0.37 mmol) were solubilized in dry THF (8 mL) under magnetic stirring in a round-bottom flask, and then SA (740 mg, 7.4 mmol) was added to the above mixture and stirred until completely dissolved. The above reaction mixture was agitated for 42 h at 25 ± 2 °C, and then samples were further concentrated by vacuum centrifugation and dissolved in 10 mL of distilled water. The pH of the resultant solution was adjusted to pH 9−10 by using $K_2CO_3$. The above reaction mixture was filtered to remove the unreacted reactants. Further, the filtrate was adjusted to pH 1−2 with dil. HCl. The formed precipitate was separated and dried to get Egen-COOH (1265.5 mg, 92% yield).[34]

*Conjugation of CS with Activated Egen-COOH.* Carbodiimide chemistry was used for the preparation of the Egen-COOH conjugated CS (CS-*g*-Egen) graft polymer. The conjugation reaction was mediated by NHS/EDC. The mixture of Egen-COOH (160 mg, 0.6 mmol), NHS (69 mg, 0.6 mmol), and EDC (115 mg, 0.6 mmol) was transferred into anhydrous dichloromethane (DCM) and stirred by a magnetic stirrer (REMI 1 MLH) at room temperature. Following the evaporation of DCM, the residue was transferred to the solution of CS in 1% v/v glacial acetic acid at pH 4. The reaction was finished after 24 h, and the graft polymer was lyophilized (Labocon 4.5 L, United Kingdom) after being dialyzed for 72 h against distilled water to eliminate any remaining free reactants.[22]

*Characterization of the CS-g-Egen Conjugate.* CS, Egen, Egen-COOH, and CS-*g*-Egen were characterized by FTIR, NMR, and mass spectroscopy for their identification and confirmation of Egen-COOH and CS-*g*-Egen synthesis.

*Degree of Egen Substitution.* The degree of Egen substitution on CS was estimated with the help of a multimode microplate reader (Molecular Devices, USA). Preferentially, the CS-*g*-Egen (4 mg) sample was sonicated in a water bath sonicator for 4 h in a solution of DMSO/DCM (8:2). The vortexed samples were subjected to centrifugation (REMI Cooling Centrifuge) for 30 min at 10,000 rpm and then filtered and analyzed in the UV mode of the microplate reader. The concentration of Egen in the sample was estimated by using a standard calibration curve of Egen plotted at $\lambda_{max}$ of 296 nm.[35,36] The following formula was used for the calculation:

$$\text{Degree of Egen substitution} = \frac{\text{Egen/MWEgen}}{\text{(CSEgen} - \text{Egen)/MWCS}} \quad (1)$$

where Egen indicates the concentration of estrone in the sample, MWEgen is the molecular weight of Egen, CSEgen represents the amount of CS-*g*-Egen used in this experiment, and MWCS is the molecular weight of CS.

**Preparation of NPs.** The PLB loaded nontargeted nanoparticles (PLB-CS NPs) and targeted nanoparticles (PLB-CS-*g*-Egen NPs) were formulated by modified solvent evaporation with an ionic cross-linking method.[35] Briefly, 30 mg of the CS was dissolved in 4 mL of the 0.2% v/v glacial acetic acid solution, and the pH of the mixture solution was raised to pH 5.5 with the help of NaOH. Further, 20 mg of the TPGS was dissolved in the above solution. Concisely, 1 mL of chloroform containing 3 mg of PLB was transferred to the above CS solution under ultrasonication, and an emulsion was made by utilizing an ultrasonic homogenizer (Hielscher UP200H, Germany). The ultrasonic homogenizer was set at an amplitude of 60%, and emulsification was performed for 3 min. The formed emulsion was subjected to magnetic stirring for 4 h to complete the evaporation of the chloroform, and then 1 mL of the solution of sodium tripolyphosphate (sod. TPP, 1 mg/mL) was added dropwise to the NP suspension for the cross-linking under magnetic stirring. The larger NPs were removed by centrifugation at 3000 rpm for 5 min. Further, the NP suspension was subjected to centrifugation at 10,000 rpm for 15 min, the transparent supernatant was discarded, and the NP pellets were washed with distilled water. The pellets were redispersed in 10 mL of normal saline (pH 7.4).

Targeted NPs were prepared in a similar manner by replacing 10 mg of CS with 10 mg of CS-*g*-Egen. Similarly, CM6 loaded NPs of all CS NPs were prepared by replacing PLB with 0.3 mg of CM6 for the cellular uptake study. Further, 2 μg DiD was used instead of PLB for the preparation of the DiD-CS NPs and DiD-CS-*g*-Egen NPs by a similar process for the *in vivo* fluorescence imaging study in the rats. The composition of the various NPs formulation is presented in Table 1.

**Table 1. Composition of the Various NP Formulations[a]**

| batches | CS (mg) | TPGS (mg) | CS-*g*-Egen (mg) | palbociclib (mg) | CM6 (mg) | sod. TPP (mg) |
|---|---|---|---|---|---|---|
| blank CS NPs | 30 | 20 | | | | 1 |
| PLB-CS NPs | 30 | 20 | | 3 | | 1 |
| PLB-CS-*g*-Egen NPs | 20 | 20 | 10 | 3 | | 1 |
| CM6-CS NPs | 30 | 20 | | | 0.3 | 1 |
| CM6-CS-*g*-Egen NPs | 20 | 20 | 10 | | 0.3 | 1 |

[a]Blank CS NPs: blank chitosan nanoparticles; PLB-CS NPs: nontargeted PLB loaded chitosan nanoparticles; PLB-CS-*g*-Egen NPs: estrogen receptor targeted PLB loaded chitosan nanoparticles; CM6-CS NPs: nontargeted coumarin-6 loaded chitosan nanoparticles; and CM6-CS-*g*-Egen NPs: estrogen receptor targeted coumarin-6 loaded chitosan nanoparticles.

**Characterization of Nanoparticles.** *Particle Size, Zeta Potential, and Polydispersity Index.* The prepared NPs were evaluated for their mean particle size and zeta potential by using a Zetasizer (Nano ZS90, Malvern Instruments). All the values reported are the means of the three values. Particle size analysis was based on dynamic light scattering (DLS), and zeta potential was analyzed on the basis of the electrophoretic mobility of the particles under electric fields.[37]

*Entrapment Efficiency and Drug Loading Capacity.* The percentage of the entrapped drug inside the NPs was estimated by using a validated RP-HPLC (Shimadzu LC-20AR, Japan) analytical method.[38] Briefly, 0.2 mL of the NP suspension was evaporated in a rotary evaporator, and the residue was dispersed in 1 mL of methanol and sonicated in a water bath sonicator for 1 h to break the NPs. The samples were centrifuged at 10,000 rpm for 15 min, filtered through a 0.22 μm nylon filter, and analyzed by HPLC after suitable dilution in the mobile phase. The standard calibration curve of the PLB was linear in the range of 10−60 ng/mL ($R^2$ = 0.9994). The HPLC method was used for the PLB analysis consisting of mobile phase A: acetonitrile and mobile phase B: methanol in the ratio of 30:70. The chromatographic conditions for the RP-HPLC analysis were 1 mL/min flow rate, 100 μL injection volume, 4.8 min retention time, and a photodiode array detector ($\lambda_{max}$ = 355). A Shimadzu Shim-pack C18 column was used in the HPLC.

The percentage entrapment of the CM6 in the NPs was calculated by using the fluorescence mode of the microplate reader. After the sample preparation, readings were taken in the fluorescence mode with excitation at 462 nm and emission at 502 nm in chloroform, and a standard curve was linear (10−100 ng/mL) with $R^2$ = 0.999.

The entrapment efficiency (EE) was estimated by using the following equation:

$$\text{Entrapment efficiency(\%)} = \frac{\text{amount of the drug entrapped in the NPs}}{\text{amount of the drug used in the NP preparation}} \times 100 \quad (2)$$


https://doi.org/10.1021/acsami.3c03184
ACS Appl. Mater. Interfaces XXXX, XXX, XXX−XXX

*High-Resolution Scanning Electron Microscopy (HR-SEM).* At room temperature, the morphologies of the developed PLB-CS NPs and PLB-CS-*g*-Egen NPs were captured by using a high-resolution electron microscope (Nova Nano SEM 450, FEI USA). The HR-SEM was set at 15 kV with magnification of 200 KX and 350 KX. The PLB-CS NP and PLB-CS-*g*-Egen NP suspensions were further diluted 10 times with distilled water, and a drop of the sample was casted on a separate glass slide, evenly spread, and dried for 12 h in a vacuum dryer. The prepared samples were coated with carbon, and microscopic images were captured.[39]

*High-Resolution Transmission Electron Microscopy (HR-TEM).* PLB-CS NP and PLB-CS-*g*-Egen NP images were captured by using HR-TEM (Tecnai G2 20 TWIN, FEI USA). The NP samples were diluted 10-fold with distilled water and casted on a separate carbon coated copper TEM grid with a 400 mesh size. The NP casted TEM grid was vacuum dried, and microscopic images were captured at a voltage of 100 kV.[40]

*Atomic Force Microscopy (AFM).* Additionally, two-dimensional (2D) and three-dimensional (3D) images of the NPs were captured by using AFM (NTEGRA Prima, Netherlands). A drop of NP suspensions after 10 times dilution with distilled water was casted on the individual glass slide and homogeneously distributed to form a thin film. Further, samples casted as a film were dried in the vacuum dryer under reduced pressure. The images were captured and processed by using the AFM image analysis software (Nova Px, NT-MDT Netherlands).[41]

*Surface Chemistry.* Surface chemistry analysis of the PLB-CS NPs and PLB-CS-*g*-Egen NPs was done by utilizing X-ray photoelectron spectroscopy (XPS; Thermo Scientific K-Alpha XPS System) to confirm the NP surface elemental composition in fixed transmission mode with binding energies in the range of 0−800 eV. Similarly, sample preparation for the XPS involves the casting of a suitably diluted NP suspension in distilled water on a glass slide, and after drying in the vacuum oven under reduced pressure, samples were analyzed.[23]

*Egen Surface Content.* The content of the Egen in PLB-CS-*g*-Egen NPs was calculated by a multimode microplate reader (Molecular Devices, USA). In brief, 0.2 mL of the NPs was lyophilized and transferred into a mixture of DMSO/DCM (4:1). The sample was subjected to vortexing for 4 h and centrifuged. The supernatant was collected and passed through a 0.22 $\mu$m filter, and the filtrate was analyzed in the UV−vis mode of the microplate reader at a fixed $\lambda$max = 296 nm.[42] Similarly, the total Egen content used in the NPs was determined by using 10 mg of the CS-*g*-Egen polymer. The analysis was performed without any interference from the PLB due to the wide difference in the detection $\lambda$max of PLB and Egen. The samples were compared with the standard calibration curve of Egen. The total Egen content in the PLB-CS-*g*-Egen NPs was determined by the following formula:

$$\text{Egen surface content (\%)} = \frac{\text{Egen content determined in the nanoparticles}}{\text{total Egen content used in the nanoparticles}} \times 100 \quad (3)$$

*X-ray Diffraction Study.* X-ray diffraction (XRD) is the characterization technique used for the observation of any crystalline peaks in the excipients, drugs, and their formulations. The physical state of the drug in the formulation was determined by using a Rigaku MiniFlex X-ray diffractometer. A voltage of 40 kV and a current of 15 mA were applied to the samples, 5−50° was the sample scanning range (2$\theta$), and the scan speed was 7°/min.[43]

**In Vitro Studies.** *In Vitro Drug Release.* The *in vitro* drug release of the PLB from the NPs was evaluated in phosphate buffer saline (PBS pH 7.4) and acetate buffer (pH 5.5). The principle of dialysis bag diffusion was applied for the understanding of the PLB release behavior from the NPs. The volume of the NPs equivalent to 0.3 mg PLB was transferred to a dialysis bag (1 kDa, MWCO), sealed hermetically, and immersed into 100 mL of the release medium. The system was maintained at 37 ± 5 °C with continuous shaking at 100 rpm. An equal volume of the fresh release medium was replaced after each predetermined sampling time point from the receptor compartment. The collected samples were appropriately diluted and filtered through a 0.22 $\mu$m PVDF filter before being collected into the HPLC vials. *In vitro* release of the PLB was calculated by HPLC; the analytical method was similar to that used for the calculation of entrapment efficiency.[22]

*Hemolysis and Hemocompatibility Study.* The compatibility of the developed formulation with human blood was evaluated for the understanding of the effect of the NPs on the red blood cells. A sample of 5 mL blood was collected from the blood bank in a tube containing EDTA, and RBCs were separated by centrifugation at 2000 rpm. The formed pellets of the RBCs at the bottom of the centrifuge tube were washed two to three times with normal saline and suspended in normal saline. Further, 900 $\mu$L of RBC suspension was incubated with 100 $\mu$L of various formulations (i.e., PLB, PLB-CS NPs, and PLB-CS-*g*-Egen NPs). For positive control, RBCs were suspended in distilled water, whereas negative control or blank RBCs were suspended in normal saline. These samples were incubated at 37 °C for 1 h under gentle shaking. The distilled water causes 100% hemolysis due to the permeation of the water to the RBCs, causing them to swell and burst. After incubation, a drop of the samples was casted on the separate glass slides, and the smear was prepared and stained with Leishman stain. After completion of the staining procedure, images of the stained RBCs were captured by using a bright microscope. Further, incubated samples were centrifuged for 5 min at 2000 rpm. The supernatant of the samples was collected, and absorbance was measured at 540 nm using a multimode microplate reader (UV−vis mode). As per the ASMT E2524-22 testing method for the hemolysis of the NPs, the negative control should not be more than 2%, and if the hemolysis % of the test materials is more than 5%, it indicates that they may cause hemolysis if administered intravenously.[44]

$$\%\text{Hemolysis} = \frac{\text{Abs test} - \text{Abs negative control}}{\text{Abs positive control} - \text{Abs negative control}} \times 100 \quad (4)$$

*Cell Culture and Cell Line Maintenance.* Mammalian breast cancer cell lines T47D and MCF7 were cultured in Dulbecco's modified Eagle medium (DMEM) containing 10% fetal bovine serum (FBS) along with penicillin−streptomycin antibiotic solutions. The cells were grown in a humidified $CO_2$ incubator, and 5% $CO_2$ was supplied throughout the experimentation.

*In Vitro Cytotoxicity Assay.* The *in vitro* cytotoxicity activity of the free PLB, PLB-CS NPs, and PLB-CS-*g*-Egen NPs was evaluated in the estrogen overexpressed breast cancer cell lines (T47D and MCF7). Briefly, $1 \times 10^4$ cells were seeded in each well of 96-well cell culture plates in DMEM and maintained overnight in a $CO_2$ humidified incubator (5% $CO_2$) at 37 ° C. After overnight incubation, utilized media were eliminated, and the cells were treated with the free drug PLB-CS-*g*-Egen NPs at different concentrations (0.01, 0.1, 1, 10, and 100 $\mu$g/mL), diluted in DMEM, and incubated for 24 h. After drug incubation, the drug containing medium was discarded, and fresh MTT containing medium was added into each well and incubated for 4 h. The treatment medium was gently shaken without disturbing the formazan crystal. Additionally, crystals were washed and dried for an additional 2 h followed by washing and drying for another 2 h. Finally, 100 $\mu$L of DMSO was added into each well and gently shaken on the gyratory shaker for 30 min. Afterward, the optical density of the samples was taken at 570 nm by using a microplate reader (Multiplate reader, BioRad).[45] Similarly, % cellular viability of MCF7 and T47D cells was estimated after treatment with blank nontargeted NPs and blank targeted NPs. The percentage cellular viability was estimated by using the following formula:

$$\%\text{Cellular viability} = \frac{\text{absorbance of the treated cells}}{\text{absorbance of the control cells}} \times 100 \quad (5)$$

**Cellular Uptake Study.** The cellular uptake of free CM6, CM6-CS NPs, and CM6-CS-*g*-Egen NPs was studied in the MCF7 cell line


https://doi.org/10.1021/acsami.3c03184
ACS Appl. Mater. Interfaces XXXX, XXX, XXX−XXX

by confocal microscopy (super resolution confocal microscopy, Leica, Germany). In brief, $1 \times 10^5$ MCF7 cells were grown for 24 h on a cover slip in six-well cell culture plates. Then, cells were incubated with each of the free CM6, CM6-CS NPs, and CM6-CS-*g*-Egen NPs at 5 $\mu$g/mL concentration for 2 h. Then, cells were washed two times with cold PBS. After incubation, the cells were fixed with 4% paraformaldehyde. Further, cells were again washed three times with cold PBS. Fixed cell nuclei were stained by incubation with propidium iodide (PI) for another 30 min. For the receptor blocking study, cells were treated with free Egen (2 mg/mL) prior to 6 h of treatment with CM6-CS-*g*-Egen NPs. Finally, the cell monolayers were captured by using confocal microscopy.[45]

**Apoptosis Study with Hoechst/PI Dual Staining.** The apoptotic potential of free drug and receptor mediated drug delivery was determined by the Hoechst 33342/PI dual stating method. Briefly, $1 \times 10^5$ MCF7 and T47D cells were seeded separately in 12-well cell culture plates separately. Then, cells were treated with free PLB, PLB-CS NPs, and PLB-CS-*g*-Egen NPs for 24 h at 37 °C in $CO_2$. For the receptor blocking study, cells were treated with 2 mg/mL of free Egen prior to 6 h of PLB-CS-*g*-Egen NP treatments. After 24 h of incubation, the drug containing medium was discarded, and the cells were stained with a 10 $\mu$g/mL concentration of Hoechst/PI and incubated for 30 min. Then, the cells were washed with PBS, and finally, images were taken by a fluorescence microscope (EVOS FL live cell imaging system) at 40×.[46]

**Cell Cycle Analysis.** Cell cycle analysis of free PLB, PLB-CS NPs, and PLB-CS-*g*-Egen NPs was performed in MCF7 cell lines.[47] In brief, $1 \times 10^5$ MCF7 cells were seeded in a six-well cell culture plate and allowed to grow. Then, cells were incubated separately with free PLB, PLB-CS NPs, and PLB-CS-*g*-Egen NPs for 24 h. After incubation, the cells were harvested with 1 mM EDTA in cold PBS followed by fixing with 75% ethanol (ice cold). After fixation, the cells were kept at −20 °C overnight, and then, the cells were incubated with a mixture of 1 $\mu$g/mL of PI, 0.1% of Triton-X, and 200 $\mu$g/mL of RNase A. The stained cells were maintained at room temperature in the absence of light for 30 min prior to analysis. Finally, the cells were subjected to flow cytometry for the analysis (CytoFLEX S N2-V4-B2-Y4, Beckman Coulter, United States).

***In Vivo* Studies.** *Pharmacokinetic Study.* Female Sprague-Dawley (SD) rats weighing 150−200 g and 45−60 days old were procured from the animal house of IMS BHU, India. All the experimental protocols related to the animal studies (three rats per group) were approved by the Institutional Animal Ethics Committee (IAEC), IIT BHU, India. All the rats were maintained at room temperature and supplied with water and standard rat feed under natural light/dark conditions for 1 week before experiments. All the rats were randomly segregated into four groups, and each group consisted of three animals each ($n$ = 3). The first group of rats was given blank NPs intravenously, the second group of rats was administered with an intravenous injection of free PLB (suspension in sterile normal saline), the third group of rats was administered with PLB-CS NPs, and the fourth group received PLB-CS-*g*-Egen NPs.[22] Prior to the intravenous injections, all the nanoparticles were passed through a 0.45 $\mu$m syringe filter followed by terminal sterilization under UV light for 2 h. Intravenous injection of the different formulations was given at a dose of 5.91 mg/kg body weight. Following the administration of the different formulation, 0.4 mL of blood from rats was collected in heparinized tubes under mild anesthetic conditions. The sampling time points of blood collections were 0.5, 1, 2, 4, 8, 12, 24, and 48 h. Plasma from each sample was separated by centrifugation (5000 rpm, 5 min) at 4 °C. The plasma protein was precipitated by the addition of an equal volume of acetonitrile to the plasma samples. Further, samples were centrifuged at 15,000 rpm (10 min) to remove the precipitated protein. Finally, the supernatant was collected, filtered through a syringe filter, and analyzed by a validated HPLC method after suitable dilution with the mobile phase.

*Histopathology Study.* The safety of the prepared formulations was analyzed by a histopathological study to report any toxicity that appeared after multiple administrations of the formulation to the rats ($n$ = 3). The PLB 5.91 mg/kg rat dose was fixed by considering the reported 125 mg of PLB adult dose, 46% of oral bioavailability, and metabolic rate in the rats. The rats were randomly segregated into four groups with three animals in each group. Intravenous injections of saline (vehicle control), free PLB (drug control), PLB-CS NPs (nontargeted NPs), and PLB-CS-*g*-Egen NPs (targeted NPs) were done at a dose of 5.91 mg/kg at an interval of 3 days. On the 15th day, all rats were sacrificed, and vital organs (brain, lungs, liver, kidney, and spleen) were isolated. The organs were washed with normal saline and fixed in the mounting medium for cryostat. The samples were sectioned in a cryomicrotome (Leica CM1950) having 5 $\mu$m thickness. The sample sections were stained with hematoxylin and eosin (H & E) dye.[48] All the stained specimens were mounted on glass slides for visualization under a bright microscope, and images were captured by using a Dewinter microscope (Capture Pro 4.1 software).

***In Vivo* Antitumor Activity.** *Animals.* Female SD rats (150−200 g body weight, 45−60 days of age) were maintained at room temperature under standard conditions and foods. All the procedures performed on the animals were approved by IAEC, IIT BHU, Varanasi, India.

*Tumor Induction.* For the induction of the breast tumor, 5 mg of 7,12-dimethylbenz(*a*)anthracene (DMBA) was dissolved in 0.5 mL of vehicle (sunflower oil) and administered subcutaneously to the rat mammary pad on either side. All rats were screened for the development of tumor at the beginning of the 8 weeks of DMBA treatment. The screening involves palpitation of the mammary pad for the development of any abnormal mass. Tumor yield and size were stabilized after 75 days (approx.) of DMBA treatment.[49−51] Rats were kept palpitated, and when tumor size ranged from 5 to 8 mm, they were analyzed for the *in vivo* anticancer activity. DMBA induced breast tumors are overexpressed with hormonal receptors such as ER and PR,[52] and also the cell line derived from the DMBA induced breast tumors exhibits a similar nature to that of the MCF7 cell line.[53]

*Histological Identification of the Tumor.* The developed tumor from a rat (DMBA treated) was harvested and washed with normal saline. The tumor was fixed in paraffin wax, and a 5 $\mu$m thick section was prepared by using a microtome. As of today, H & E staining is the gold standard technique for the differentiation of the tumor from the normal tissue. The obtained tumor section was stained with H & E stain as per the standard protocol, and a slide was prepared. Similarly, a normal rat breast pad was isolated, and H & E staining was performed for comparison with breast tumor.

Additionally, a prepared paraffin block of the tumor was sectioned to get a 5 $\mu$m thick tissue and treated with ER antibody as per the standard protocol of immunohistochemistry for the detection of ER expression. The prepared specimen was subjected to ER scoring. As per the College of American Pathologist (CAP) guideline for ER scoring, ≥1% immunoreactive tumor cells are considered as positive for ER, whereas <1% is considered as negative.[54]

*In Vivo Antitumor Study by Ultrasound and Photoacoustic Imaging.* Female SD rats that had DMBA induced breast cancer were used for the *in vivo* antitumor study. Breast tumor induced rats were randomly distributed into four groups, with each group containing three rats ($n$ = 3). All the animals with breast tumor were scanned by using ultrasound and a photoacoustic imaging system (Vevo LAZR_X Vevo 3100 imaging system, Toronto, Canada) equipped with a 40 MHz ultrasound array transducer prior to the treatment with NPs.[55,56] The scanning of the breast tumor was performed in B-mode (ultrasound mode), power Doppler mode (for vascularity), and photoacoustic mode. All the animals received intravenous dosing of the free drug and NPs (5.91 mg/kg body weight). The first group (control) received no treatments, the second group received PLB (drug control), the third group received PLB-CS NPs, and the fourth group received PLB-CS-*g*-Egen NPs. Photoacoustic and ultrasound images of the breast tumors were visualized at 0, 2, 4, and 8 days after treatments. For the visualization of the tumor area in ultrasound and photoacoustic analysis mode, the tumor area was irradiated with a 700 nm, 40 MHz pulse repetition frequency. The captured ultrasound and photoacoustic images were overlaid to determine the size, shape, and


https://doi.org/10.1021/acsami.3c03184
ACS Appl. Mater. Interfaces XXXX, XXX, XXX−XXX

Table 2. PS, PDI, ZP, EE, and $IC_{50}$ Value of Developed NPs[a]

| batches | PS (mean ± SD[b]) | PDI (mean ± SD[b]) | ZP (mV) (mean ± SD[b]) | EE (mean ± SD[b]) | $IC_{50}$ (μg/mL) (mean ± SD[b]) MCF7 | T47D |
|---|---|---|---|---|---|---|
| PLB | | | | | 41.86 ± 1.53 | 48.32 ± 1.296 |
| blank CS NPs | 101.2 ± 2.73 | 0.198 ± 0.058 | 19.90 ± 0.568 | | | |
| PLB-CS NPs | 116.3 ± 1.53 | 0.240 ± 0.032 | 18.70 ± 0.416 | 72.93 ± 1.297 | 3.45 ± 0.45 | 6.29 ± 0.67 |
| PLB-CS-*g*-Egen NPs | 141.6 ± 1.97 | 0.220 ± 0.042 | 12.45 ± 0.574 | 75.79 ± 2.195 | 0.73 ± 0.07 | 1.59 ± 0.0.08 |
| CM6-CS NPs | 110.2 ± 1.27 | 0.240 ± 0.022 | 17.20 ± 0.354 | 86.69 ± 1.675 | | |
| CM6-CS-*g*-Egen NPs | 135.3 ± 1.41 | 0.250 ± 0.014 | 11.38 ± 0.251 | 84.47 ± 2.161 | | |

[a]Blank CS NPs: blank chitosan nanoparticles; PLB-CS NPs: nontargeted PLB loaded chitosan nanoparticles; PLB-CS-*g*-Egen NPs: estrogen receptor targeted PLB loaded chitosan nanoparticles; CM6-CS NPs: nontargeted coumarin-6 loaded chitosan nanoparticles; CM6-CS-*g*-Egen NPs: estrogen receptor targeted coumarin-6 loaded chitosan nanoparticles; PS: particle size; PDI: polydispersity index; ZP: zeta potential; and EE: entrapment efficiency. [b]$n = 3$; SD: standard deviation.

oxygenation level of the tumor. Power Doppler images were analyzed to check tumor vascularity and angiogenesis. All the images were processed by using the Vevo LAB software (FUJIFILM VisualSonics, Toronto, Canada).

Additionally, similar treatment groups of rats (control, PLB, PLB-CS NPs, and PLB-CS-*g*-Egen NPs), including healthy rats (negative control), were used separately for survival time analysis. The survival study was performed for 6 months. During the study period, the health condition of the rats was monitored weekly. The percentage survival of rats was calculated, and the Kaplan−Meier survival curve was plotted.[57]

*In Vivo Breast Tumor Targeting Efficiency by IVIS Live Imaging.* *In vivo* fluorescence imaging of free DiD (control), DiD-CS NPs, and DiD-CS-*g*-Egen NPs was performed on DMBA induced breast tumor in rats using the Photon Imager Optima System (Biospace Lab). The free DiD and DiD loaded NPs equivalent to 200 nM of DiD dye were administered intravenously by the tail vein to the rats, and the fluorescence signals were captured at excitation and emission wavelengths of 620 and 710 nm, respectively, at 2, 4, 6, and 8 h postinjection. The radiant efficiency (measured as fluorescence intensity/area/time) was analyzed using the Biospace Lab imaging software by the region of interest (ROI) tool, in circled the breast tumor area.[23]

**Statistical Analysis.** Data from the *in vitro* and *in vivo* experiments were presented as the mean ± SD ($n = 3$). GraphPad Prism 7.0 was used for the statistical calculation. One-way ANOVA and the *t* test were used for the calculation of the statistical significance among groups. The statistically significant level was considered as ns ($p \geq 0.05$), * ($p < 0.05$), ** ($p < 0.01$), *** ($p < 0.001$), and **** ($p < 0.0001$).

## RESULTS AND DISCUSSION

**Characterization of the CS-*g*-Egen Conjugate.** *FTIR.* The FTIR spectra of CS, Egen, Egen-COOH, and CS-*g*-Egen were compared to analyze the synthesized Egen-COOH and CS-*g*-Egen, as shown in Figure S1. Egen demonstrated the FTIR peaks of OH, C−H, C═O (ketone), C−O, and C═C (aromatic) stretching peaks at 3360, 2909, 1718, 1240, and 1556 $cm^{-1}$. Egen-COOH showed OH, C−H, C═O (ester), C−O, and C═C (aromatic) stretching vibrations at 3303, 2943, 1725, 1285, and 1658 $cm^{-1}$, respectively. A slight shift in the FTIR peak of Egen was observed after carboxylation and formation of the ester bond. Meanwhile, CS-*g*-Egen demonstrated OH, C−H, C═O (amide), C−O, and C═C (aromatic) stretching vibrations at 3360, 2898, 1678, 1217, 1048, and 1556 $cm^{-1}$, respectively, and NH bending vibrations at 1624 $cm^{-1}$. When Egen-COOH was conjugated with CS, the formation of the amide bond was observed, which led to a slight shift in the FTIR peaks. Table S1 in the Supporting Information shows all the characteristic peaks related to their functional groups.

*NMR.* Figure S2 displays the $^1H$ NMR spectra of CS, Egen, Egen-COOH, and CS-*g*-Egen. The spectra of CS displayed the peak of the $NH_2$ functional group at 1.8−2 ppm, whereas these peaks were absent in the spectra of Egen-COOH because of the substitution. However, the spectra of Egen-COOH also displayed the peaks of methylene protons of the conjugated succinate group at 3 ppm and aromatic protons of estrogen at 6.5 and 7 ppm. Moreover, the spectra of CS-*g*-Egen consist of the characteristic peak NH of the amide linkage at 8.3 ppm and aromatic protons at 6.5, 7, and 7.6 ppm. All these findings support the successful conjugation of CS-*g*-Egen.

*High-Resolution Mass Spectroscopy.* The synthesized Egen-COOH and its conjugate with CS (CS-*g*-Egen) were examined by time-of-flight mass spectroscopy (Figure S3A,A1,A2,B). Egen was functionalized with −COOH by the process of succinylation. The molecular weight of Egen was 270.4 g/mol, and after succinylation, it was increased to 370.4 g/mol. The molecular ion peaks of Egen-COOH (M + 1) were at *m*/*z* of 371.18 (Figure S3A), and the M + 2 peak was observed at *m*/*z* of 372.19 (Figure S3A2). The formation of the amide linkage between the carbonyl carbon of Egen-COOH and the amino group of CS releases a molecule of water. The molecular weights of CS and Egen-COOH were 1526.5 and 370.4 g/mol, respectively. The molecular weight of CS-*g*-Egen was approximately 1878.9 g/mol, and the molecular ion peaks (M + 1, M + 2, M − 1, and M − 2) in the spectra of CS-*g*-Egen appeared at *m*/*z* 1879.25, 1880.76, 1878.21, and 1877.33, respectively. The HRMS analysis (Figure S3) demonstrated the successful formation of Egen-COOH and conjugation of CS with Egen to form the CS-*g*-Egen graft polymer.

*Degree of Egen Substitution.* The degree of substitution of Egen to CS was found to be 0.82 ± 0.02. The degree of conjugation can be a maximum of 1, which indicates that one molecule of Egen successfully substituted for one molecule of CS. In this case, we obtained 0.82 degree of substitution, which indicates that 82% of the CS molecules have an Egen substitution.

**Nanoparticle Characterization.** *PS, PDI, and ZP of NPs.* The characterization of the NPs is presented in Table 2. The developed NPs showed hydrodynamic diameters ranging from 101.2 ± 2.73 to 141.6 ± 1.97 nm. The obtained particle size data demonstrated that developed NPs were in the range of 100−150 nm in size. The blank CS NPs were found to have a size of 101.2 nm and a zeta potential of 19.90 mV, whereas PLB loading significantly ($p < 0.001$) increased the particle size (116.3 nm) and caused a slight reduction ($p > 0.05$, ns) in the zeta potential (18.70 mV) of nontargeted NPs as a result of the


https://doi.org/10.1021/acsami.3c03184
ACS Appl. Mater. Interfaces XXXX, XXX, XXX−XXX

entrapment of the PLB in the polymeric matrix of CS. Additionally, in the case of targeted NPs, because of the incorporation of CS-*g*-Egen, significantly ($p < 0.001$) increased particle size (141.6 nm) and reduced zeta potential (12.45 mV) were observed. The increase in size was attributed to the presence of Egen (targeting moiety) on the NP surfaces, whereas the decrease ($p < 0.001$) in the zeta potential was mainly due to the presence of a low number of free $NH_2$ compared to nontargeted NPs. A statistical comparison of PLB, PLB-CS NP, and PLB-CS-*g*-Egen NP particle size and zeta potential is presented in Figure S4A,B.

*Determination of Entrapment Efficiency.* The amounts of drug entrapped in PLB-CS NPs and PLB-CS-*g*-Egen NPs were 72.93 ± 1.997 and 75.7 9 ± 2.195%, respectively (Table 2). Preconjugation of Egen did not significantly impact the EE of the targeted NPs. Similarly, the EEs of the CM6 in the CM6-CS NPs and CM6-CS-*g*-Egen NPs were found to be 86.69 ± 1.675 and 84.47 ± 2.161%, respectively. The entrapments of the PLB or CM6 in the nontargeted NPs and targeted NPs were not significantly ($p \geq 0.05$) different from each other.

*FE-SEM.* The morphology of the prepared NPs was analyzed by FE-SEM (FEI Pvt. Ltd., USA), and images were captured for PLB-CS NPs and PLB-CS-*g*-Egen NPs. Figure 1A demonstrates that developed NPs had a spherical morphology, a smooth texture, and uniformly dispersed particles. Targeted NPs were slightly bigger in size compared to nontargeted NPs. Additionally, nontargeted NPs had completely smooth surfaces, whereas targeted NPs showed slightly rough surfaces that may be due to the presence of Egen on the surface of the targeted NPs.[58]

*TEM.* TEM uses an electron beam to capture images of the NPs. This technique provides a higher resolution for images. Figure 1B depicts TEM images of NPs with a 200 and 100 nm scale. Images of nontargeted NPs and targeted NPs showed a completely spherical shape.

*AFM.* AFM provides two-dimensional (2D) and three-dimensional (3D) topography of the NPs. It is a nonoptical imaging technique that provides high-resolution images of the NPs. The 2D and 3D AFM images in Figure 1C,D show that nontargeted NPs and targeted NPs were spherical in shape with a uniform particle size distribution. Additionally, targeted NPs appear to be slightly bigger in size compared to nontargeted NPs.

*Surface Chemistry by XPS.* X-ray photoelectron spectroscopy (XPS) was used to investigate the surface chemistry of PLB-CS NPs and PLB-CS-*g*-Egen NPs. The atomic signal of C, N, and O from NPs in terms of the XPS peak is presented in Figure 2A. In the XPS survey, C1s, N1s, and O1s were detected at the binding energies of 250−300, 400−450, and 500−550 eV, respectively. The atomic percentages of C1s, N1s, and O1s in the nontargeted NPs were found to be 76.86, 2.95, and 20.19%, respectively, whereas targeted NPs showed peaks of C1s, N1s, and O1s as 73.52, 1.51, and 24.97%, respectively. The decrease in the nitrogen atomic percentage in PLB-CS-*g*-Egen NPs was due to the preconjugation of the free nitrogen of the CS with Egen, and hence, the availability of the nitrogen atom on the surface of PLB-CS-*g*-Egen NPs was less than that of PLB-CS NPs. Additionally, an increase in the O1s signal in the targeted NPs again confirmed the presence of Egen on the targeted NP surface; this was mainly due to the presence of oxygen in the structure of Egen-COOH.

*Egen Surface Content.* The quantity of Egen present on the surface of PLB-CS-*g*-Egen NPs was found to be 71.2 ± 2.0%.

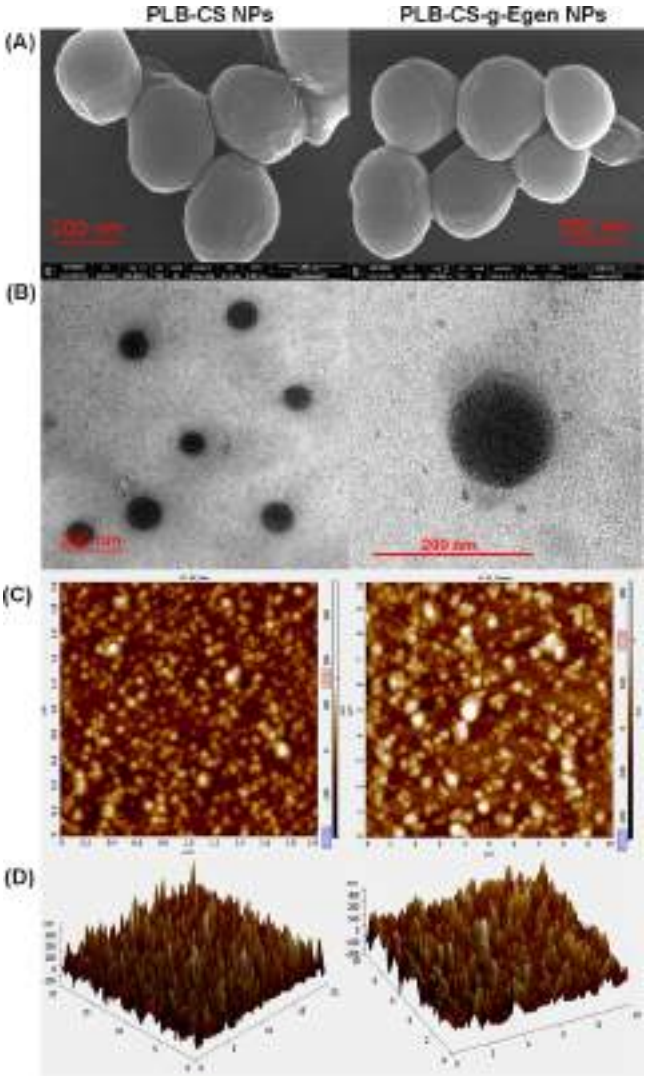


**Figure 1.** Morphological imaging of the PLB-CS NPs and PLB-CS-*g*-Egen NPs by (A) field emission scanning electron microscope (FE-SEM), (B) transmission electron microscope (TEM), (C) two-dimensional atomic force microscope (AFM), and (D) three-dimensional AFM.

The surface content of Egen is essential for the targeted delivery of PLB via receptor mediated endocytosis of the PLB-CS-*g*-Egen NPs.

*XRD Study.* An XRD study provided an understanding of the physical state of the drug in the formulation. Any changes in the physical state of the drug during the formulation of the NPs can be tracked by using XRD analysis. Most drugs exist in either crystalline or amorphous form; the amorphous form of the drug has good solubility and higher bioavailability compared to its crystalline counterpart.[59] The XRD data of PLB showed sharp multiple diffracted peaks at $2\theta$ = 7.83, 10.19, 11.35, 13.86, 17.07, 18.64, 19.86, 21.15, 22.48, and 22.95°. Pure PLB exists in the crystalline form (Figure 2B), which was in good agreement with previously reported data.[60] All the PLB peaks were absent in the nontargeted and targeted NPs, suggesting that the drug was converted into the amorphous form following the NP preparations. Hence, the developed formulation was found to have PLB present in the molecular level inside the NPs. The amorphous form of PLB has higher bioavailability relative to its crystalline form and


https://doi.org/10.1021/acsami.3c03184
ACS Appl. Mater. Interfaces XXXX, XXX, XXX−XXX

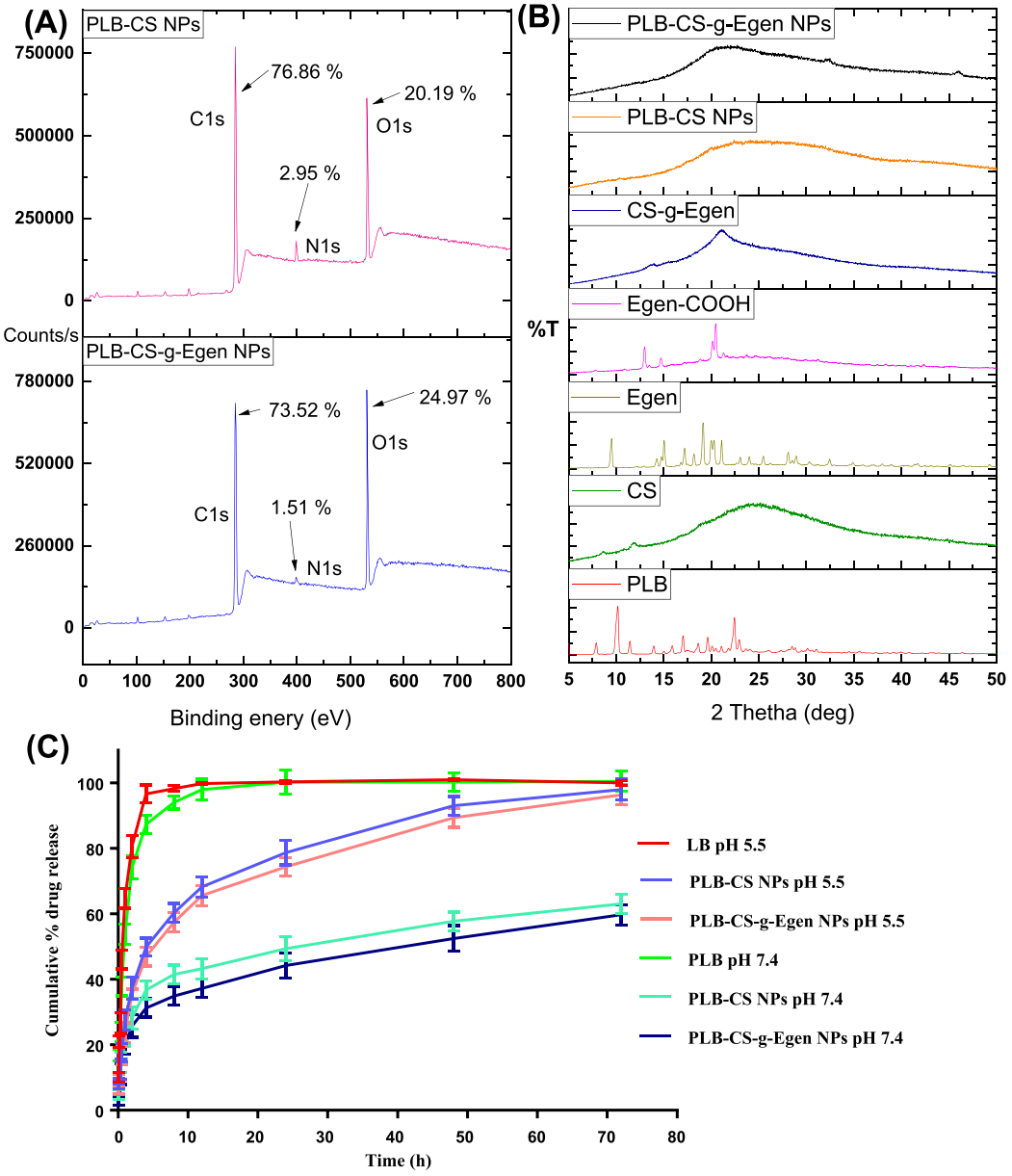


**Figure 2.** (A) X-ray photoelectron spectroscopy (XPS) analysis of PLB-CS NPs and PLB-CS-*g*-Egen NPs; (B) X-ray diffraction (XRD) spectra of PLB, CS, Egen, Egen-COOH, CS-*g*-Egen, PLB-CS NPs, and PLB-CS-*g*-Egen NPs; and (C) *in vitro* drug release profile of the PLB and NP formulations in the pH 5.5 acetate buffer and pH 7.4 phosphate buffer saline.

hence may enhance the bioavailability of PLB following NP preparation. The crystalline nature of Egen was reduced after conversion into Egen-COOH and further reduced after conjugation of CS. CS and CS-*g*-Egen polymers exist in amorphous forms as depicted in their XRD graph.

***In Vitro* Studies.** *In Vitro Drug Release Studies.* *In vitro* drug release profiles of PLB-CS NPs and PLB-CS-*g*-Egen NPs at pH 5.5 and 7.4 are presented in Figure 2C. The physiological pH of the normal human system is pH 7.4, whereas the tumor microenvironment has acidic pH (below 6.0).[61,62] $T_{50}$ is the time at which 50% of the loaded drug is released in the medium under a given set of conditions. The $T_{50}$ values of the PLB and nontargeted and targeted NPs in pH 5.5 were found to be 0.55 ± 0.05, 4.04 ± 0.22, and 5.97 ± 0.27 h, respectively, whereas the $T_{50}$ values of the PLB and nontargeted and targeted NPs in pH 7.4 were found to be 0.83 ± 0.04, 25.20 ± 0.5, and 40.80 ± 0.6 h, respectively. The $T_{50}$ value of PLB was significantly ($p < 0.001$) lower than those of targeted and nontargeted NPs at pH 5.5 and 7.4. Figure S4C,D presents the statistical comparisons of PLB, PLB-CS NP, and PLB-CS-*g*-Egen NP $T_{50}$ at pH 5.5 and 7.4.

The release profiles of PLB-CS NPs and PLB-CS-*g*-Egen NPs demonstrated a pH-dependent drug release profile. Nontargeted and targeted NPs demonstrated faster drug release at pH 5.5, which may be due to the protonation of the CS amino group increasing its aqueous solubility, and also, the drug releasing medium can easily diffuse into the NPs and promotes drug release faster. Meanwhile, at pH 7.4, protonation of CS was not feasible; hence, the NP structure remained compact, and diffusion of the drug from NPs occurred slowly. The zeta potentials of PLB-CS NPs and PLB-CS-*g*-Egen NPs at pH 5.5. were found to be 21.61 ± 0.351 and 16.52 ± 0.351 mV, respectively, which were higher than the zeta potentials of PLB-CS NPs (18.70 ± 0.416 mV) and PLB-


https://doi.org/10.1021/acsami.3c03184
ACS Appl. Mater. Interfaces XXXX, XXX, XXX−XXX

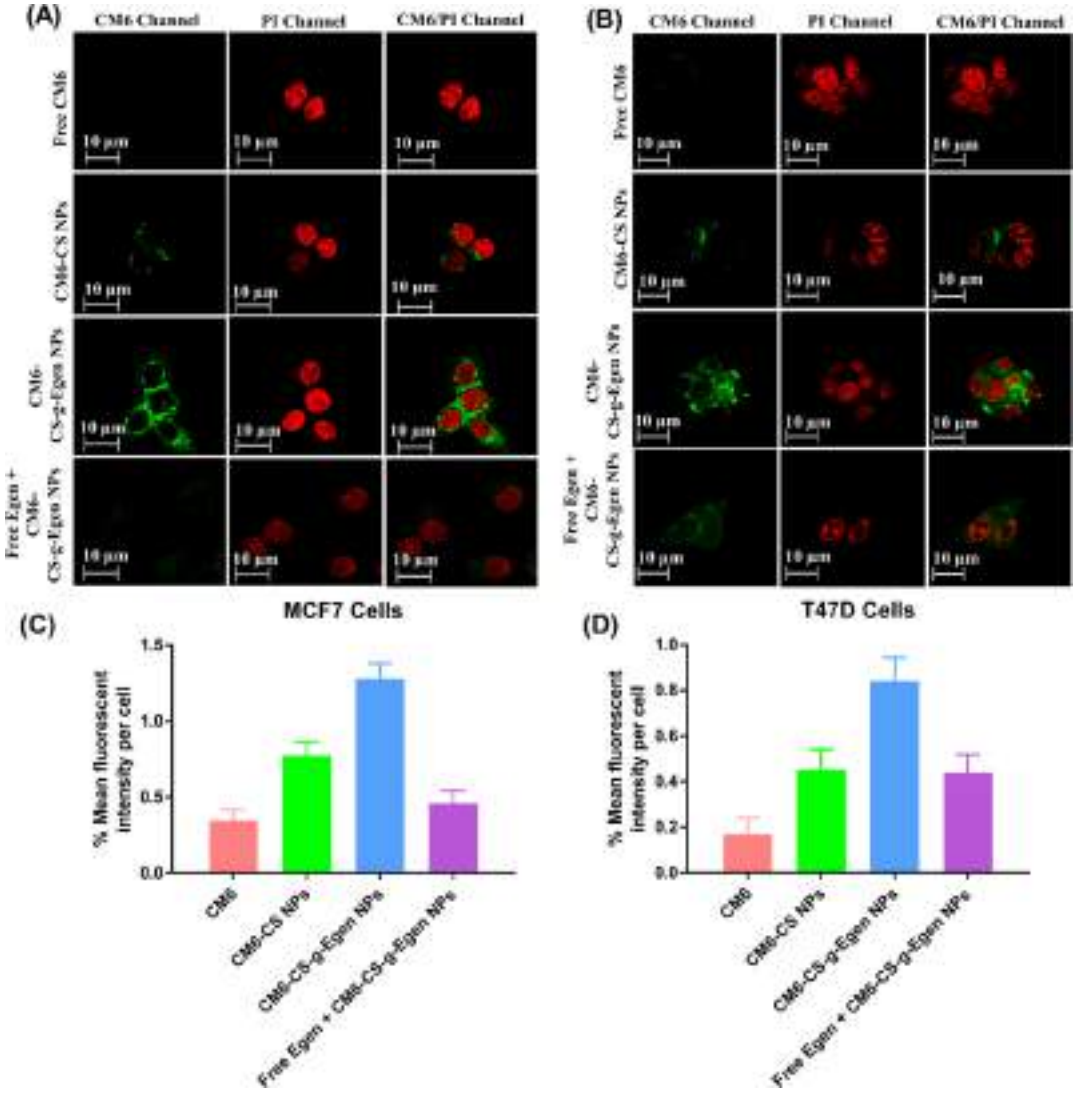


**Figure 3.** Confocal laser scanning microscopy (CLSM) images demonstrating the cellular uptake of the free CM6 (first row), CM6-CS NPs (second row), CM6-CS-*g*-Egen NPs (third row), and CM6-CS-*g*-Egen NPs after pretreatment with Egen (fourth row) in (A) MCF7 cells and (B) T47D cells. The left column (CM6 channel) shows the green fluorescence of CM6 distributed in the cytoplasm of (A) MCF7 cells and (B) T47D cells; the middle column (PI channel) shows the red fluorescence from the PI-stained nucleus; and the right column (merged) shows the CM6, CM6 loaded NPs, and PI stained nucleus. % Mean fluorescent intensity (green channel) per cell in (C) MCF7 cells and (D) T47D cells after cellular uptake of CM6, CM6-CS NPs, and CM6-CS-*g*-Egen NPs.

CS-*g*-Egen NPs (12.45 ± 0.574 mV) at pH 7.4, confirming the protonation of the NPs at pH 5.5. Free PLB release is faster in both media because of the absence of any controlling barrier except the dialysis membrane. The NPs demonstrated an initial burst release up to 2 h, which may be due to the release of drug adhered to the NP surface and the faster diffusion of drug present just beneath of NP surface. Later on, sustained release of PLB may be attributed to the slower diffusion of the drug from the NPs' inner part and core. PLB is distributed into the NPs' polymeric matrix, and hence, the drug may take a longer time to reach the NP surface.

Moreover, the pH responsive release pattern of the NPs at pH 5.5 (faster release) can be favorable for treating tumors because of its acidic microenvironment.[63]

**Hemolysis and Hemocompatibility Study.** *Blood Smear.* Nanoscale materials fall within the spectrum of viral sizes, and immunogenic proteins can stimulate the immune system, trigger an inflammatory process, and change hematological parameters.[64] We performed hematological analysis to observe any potential toxicity of PLB, PLB-CS NPs, and PLB-CS-*g*-Egen NPs. In this study, deionized water was taken as a positive control that causes 100% hemolysis, and normal saline (pH 7.4) was taken as a negative control (nonhemolytic). The blood samples were treated with different formulations and stained with Leishman stain for visualization under a bright microscope (Figure S5C) at a resolution of 40×. The obtained images depicted that treatment with PLB, PLB-CS NPs, and PLB-CS-*g*-Egen NPs did not affect the morphology of the blood cells significantly, similar to the saline-treated samples.

*Hemolytic Assay.* The hematological safety of the PLB, PLB-CS NPs, and PLB-CS-*g*-Egen NPs was analyzed by calculating the % of hemolysis that occurred after treatment with different formulations. Hemolysis %'s of PLB, PLB-CS NPs, and PLB-CS-*g*-Egen NPs were 3.761 ± 0.07, 2.035 ± 0.04, and 1.718 ± 0.10%, respectively. The results (Figure


https://doi.org/10.1021/acsami.3c03184
ACS Appl. Mater. Interfaces XXXX, XXX, XXX−XXX

S5A,B) demonstrated that PLB and nontargeted and targeted NPs were nonhemolytic to human blood.[65]

***In Vitro* Cytotoxicity Assay.** The obtained result shows that the pure drug (PLB) does not induce any significant change in cell viability at lower concentrations, whereas their encapsulation in the NP system increases their efficacy by 12.13-fold in MCF7 cells. Further, receptor mediated drug delivery of NPs was found to be more effective as compared to passive drug delivery (without receptor targeting). The $IC_{50}$ value of free PLB was found at ∼41.86 μg/mL, whereas that of PLB-CS NPs was found at ∼3.45 μg/mL, and the $IC_{50}$ value of PLB-CS-*g*-Egen NPs was found at ∼0.73 μg/mL in MCF7 cells (Figure S6A,B). In T47D cells, the $IC_{50}$ of PLB was found at ∼48.32 μg/mL, whereas the $IC_{50}$ of PLB-CS NPs was found at ∼6.29 μg/mL. Further, the $IC_{50}$ of PLB-CS-*g*-Egen NPs in T47D cells was found at ∼1.59 μg/mL (Figure S6C,D). The $IC_{50}$ value of the free PLB was in the range of the reported values in the literature.[66] So, on the basis of the obtained result, it can be concluded that the inclusion of the receptor targeting moiety in the NP system increases the potential of the drug and makes it more than ∼57-fold effective for anticancer therapy. MCF7 cells and T47D cells are overexpressed with ERs, and receptor mediated targeted PLB delivery can significantly boost the anticancer efficacy of PLB. Further, blank nontargeted NPs had ∼97 and ∼98% cellular viability in MCF7 and T47D cells, respectively, whereas blank targeted NPs had ∼96 and ∼94% cellular viability in MCF7 and T47D cells, respectively. This confirmed that blank NPs were not cytotoxic to MCF7 and T47D cells.

Recently, in a study, Parsian *et al.* developed PLB loaded magnetic dendrimers and evaluated the cellular viability of different breast cancer cells. *In vitro* cytotoxicity assays demonstrated that PLB loaded magnetic dendrimers were more sensitive to MCF7 cells relative to MDA-MB-231 cells and SKBR3 cells, reducing cellular viability by up to 30% in MCF7 cells.[67]

**Cellular Uptake Study.** Cellular uptake is a key parameter for the prediction or estimation of the therapeutic efficacy of the NPs. To enhance the cellular internalization of the NPs into the ER-positive breast tumor, active targeting via receptor mediated endocytosis has been utilized in this study. CM6 is the model dye used for the study of the NP cellular uptake in the cancer cell lines. The incubation of the CM6, CM6-CS NPS, and CM6-CS-*g*-Egen NPs with MCF7 cells and T47D cells at an equivalent dose of 5 μg/mL of CM6 demonstrated that nontargeted and targeted NPs have higher cellular uptake compared to the free CM6 (Figure 3). Additionally, targeted NPs have significantly higher fluorescence relative to non-targeted NPs, suggesting the receptor mediated cellular uptake of Egen functionalized targeted NPs. The overexpressed mER is present on the cell membrane of MCF7 cells and T47D cells, whereas ERα and ERβ are predominantly present in the cellular cytosol or nucleus.[68,69] Nontargeted NPs were internalized by cells via passive uptake that includes adhesion of the NPs (CS is positively charged) to the negatively charged cancer cells and internalization of the NPs. Additionally, nontargeted NPs show enhanced permeation and retention effects due to leaky blood vessels in the tumor microenvironments. Moreover, the functionalization of Egen on targeted NPs has added the value of receptor mediated transcytosis and passive diffusion. Nontargeted NPs were internalized into the MCF7 and T47D cells and localized in the cytoplasm of the cells (Figure 3A,B, second row), whereas targeted NPs demonstrated enhanced cellular internalization due to the presence of mER, ERα, and ERβ. Targeted NPs also demonstrated nuclear uptake of the NPs due to ERα and ERβ mediated cellular uptake (Figure 3A,B, third row). Further, receptor blocking of the MCF7 cells and T47D with free Egen demonstrated reduced cellular uptake of the targeted NPs, which confirmed the receptor mediated cellular uptake of the CM6-CS-*g*-Egen NPs. For the quantitative cellular uptake study, % mean fluorescent intensities (green channel) per cell in MCF7 cells and T47D cells after cellular uptake of CM6, CM6-CS NPs, and CM6-CS-*g*-Egen NPs were calculated by using the ImageJ software (Figure 3C,D). The % mean fluorescent intensities of CM6, CM6-CS NPs, CM6-CS-*g*-Egen NPs, and Egen pretreated + CM6-CS-*g*-Egen NPs per cell in MCF7 cells were 0.346 ± 0.07, 0.775 ± 0.09, 1.28 ± 0.102, and 0.46 ± 0.08%, respectively. Meanwhile, in T47D cells, the CM6, CM6-CS NPs, CM6-CS-*g*-Egen NPs, and Egen pretreated + CM6-CS-*g*-Egen NPs had % mean fluorescent intensities of 0.170 ± 0.07, 0.453 ± 0.09, 0.842 ± 0.101, and 0.44 ± 0.06%, respectively.

**Hoechst/PI Dual Staining for Apoptosis.** Chromatin condensation, nuclear DNA fragmentation, and cellular membrane blebbing are the major hallmarks of apoptosis after anticancer drug treatment.[70] In this study, we have used Hoechst and PI to stain the nuclei of the cells after PLB, PLB-CS NP, and PLB-CS-*g*-Egen NP treatments. Hoechst 33342 is a vital dye that stains the nuclei of both live and apoptotic cells, whereas PI only enters the cells that have compromised cellular membrane.[71] Hoechst stains the condensed chromatin more brightly in apoptotic cells compared to normal cells. The staining patterns resulting from the simultaneous use of these dyes help in the differentiation of the normal cells and apoptotic cells by using a fluorescence microscope or flow cytometer. Incubation of the MCF7 cells and T47D cells with PLB did not significantly induce apoptosis. Targeted NPs significantly promoted apoptosis in MCF7 cells and T47D cells compared to nontargeted NPs due to receptor mediated (mER, ERα, and ERβ) endocytosis of the NPs, which is also evident from MTT assay and cellular uptake study. Additionally, receptor mediated cellular internalization was further confirmed by blocking or saturating the ER of cells with free Egen and treating cells with targeted NPs. The obtained results demonstrated that a smaller number of apoptotic cells were observed in the receptor blocked group of cells after treatment with targeted NPs. Moreover, targeted NPs demonstrated a higher number of apoptotic cells in MCF7 cells compared to the T47D cells. Figure S7A presents the apoptosis study of PLB, PLB-CS NPs, and PLB-CS-*g*-Egen NPs in MCF7 cells, whereas Figure S7B presents the apoptosis study in the T47D cells.

**Cell Cycle Analysis.** Further, the process by which drug and drug loaded NPs inhibit the growth of MCF7 has been confirmed by flow cytometry analysis. PLB is a reversible inhibitor of CDK4/6. It inhibits the phosphorylation of the retinoblastoma (Rb), leading to the blocking of cell cycle progression from the G1 to S phase. After the treatment of MCF7 cells with PLB, PLB-CS NPs, and PLB-CS-*g*-Egen NPs, PI-stained cells were analyzed in a flow cytometer. The obtained data were processed by the Cytoflex software. The nontargeted and targeted NPs significantly promoted cell cycle arrest in the G1 phase by ∼1.18-fold ($p < 0.01$) and ∼1.32-fold ($p < 0.001$), respectively, compared to the free PLB (Figure 4). The obtained data from cell cycle analysis are in good


https://doi.org/10.1021/acsami.3c03184
ACS Appl. Mater. Interfaces XXXX, XXX, XXX−XXX

agreement with the MTT assay, cellular uptake, and apoptosis study.

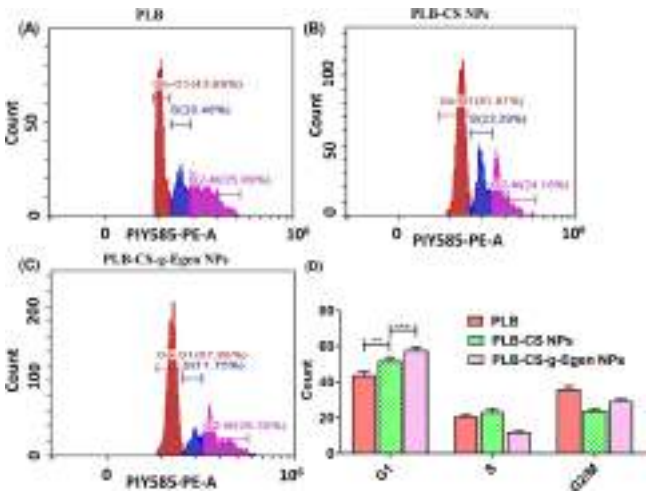


**Figure 4.** Cell cycle distribution analysis of MCF7 cells after treatment with (A) free PLB, (B) PLB-CS NPs, and (C) PLB-CS-*g*-Egen NPs. (D) Statistical comparison of the cell cycle distribution analysis of free PLB, PLB-CS NPs, and PLB-CS-*g*-Egen NPs.

**Pharmacokinetic Study.** The pharmacokinetic profiles and parameters of free PLB, PLB-CS NPs, and PLB-CS-*g*-Egen NPs are presented in Figure 5A and Table 3. The graph shows the PLB plasma concentration against time after the intravenous administration of 5.91 mg/kg equivalent dose of formulations. All the pharmacokinetic parameters were calculated by using Kinetica 5.0. Entrapment of the PLB in the NPs significantly improved the bioavailability of the PLB-CS NPs and PLB-CS-*g*-Egen NPs by 2.57- and 2.89-fold, respectively, compared to PLB. Additionally, $T_{1/2}$ of the nontargeted and targeted NPs increased by 1.90- and 1.93-fold, respectively, compared to free PLB. Further, the $AUC_{total}$ of nontargeted NPs and targeted NPs was 2.57- and 2.89-fold higher, respectively, compared to free PLB. A nonsignificant difference in pharmacokinetic parameters of nontargeted NPs and targeted NPs was observed. Overall, the incorporation of the PLB into the NPs significantly improved the pharmacokinetic profile.

**Histopathology Study.** After administration of the free PLB, PLB-CS-*g*-Egen NPs, and PLB-CS-*g*-Egen NPs at the dose of 5.914 mg/kg, vital organs (brain, lungs, liver, kidney, and spleen) were harvested and processed for H & E staining. The specimen of the different organs was observed under a microscope, and captured images are presented in Figure 5B. The obtained histopathological images of the control rat were compared with NP-treated rats to identify any toxicity associated with treatment with different formulations. Careful examination of the histopathological images of the control group of animals demonstrated that vital organs are free from pathological lesions. Meanwhile, animals receiving free PLB showed lesions in the brain, liver, lungs, and spleen. Nontargeted NPs have a slightly improved safety profile of the drug as demonstrated in the histopathological images. Finally, targeted NPs did not show any toxicity to the vital organs, and images were similar to the control group of animals.[35]

***In Vivo* Antitumor Activity.** The breast tumor induced SD rats were subjected to photoacoustic and ultrasound imaging at

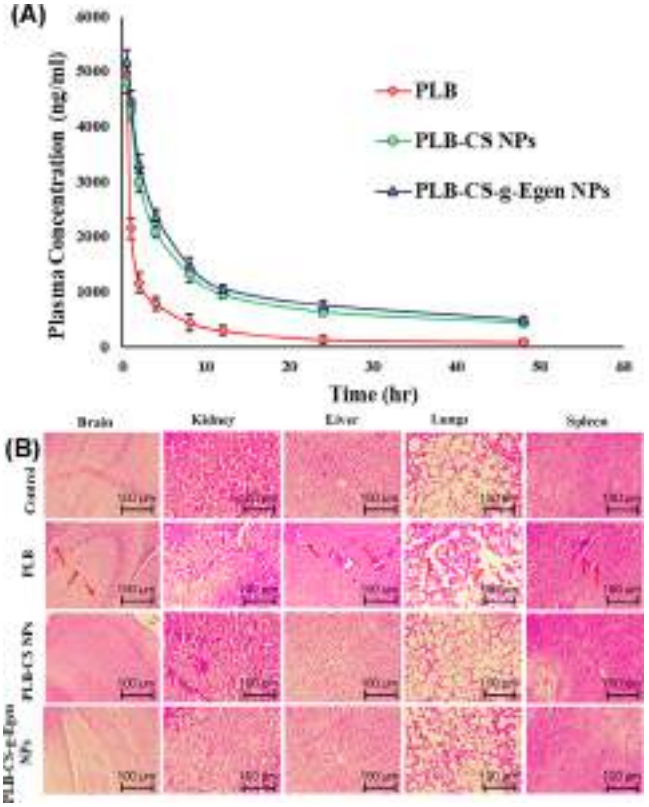


**Figure 5.** (A) Pharmacokinetic study showing the plasma concentration vs time profile of drug concentration after the intravenous administration of PLB, PLB-CS-*g*-Egen NPs, and PLB-CS-*g*-Egen NPs. (B) Histopathological images of the rats' vital organs after treatments with PLB, PLB-CS NPs, and PLB-CS-*g*-Egen NPs. Arrow (red) indicates the location of the lesion.

0 day (before treatments) and at 2, 4, and 8 days after treatments. The ultrasound/PA images of the breast tumor demonstrated a significant reduction of the breast tumor after the administration of the targeted NPs compared to the nontargeted and free PLB, whereas the tumor size was increased in the control animal receiving only saline (control group). At the eighth day, the breast tumor completely vanished in the rats receiving targeted NPs (Figure 6A,B).

Inadequate oxygen supply to the tissue, which compromises biologic functions, is known as tissue hypoxia. Hypoxia, identified as one of the signature marks of solid malignant tumors, results from a lesser oxygen supply beyond 70 to 150 $\mu$m of the tumor vasculature system developed by rapidly proliferating malignant cells.[72,73] Experimental and clinical studies provided sufficient evidence to establish a fundamental role for hypoxia in solid tumors. The pathophysiologic condition of malignant tumor leads to structurally and functionally disturbed microcirculation and the deterioration of diffusion conditions, which result in tumor hypoxia.[74] Intratumoral hypoxia, which is primarily brought on by structural and functional anomalies in the vascular endothelium, is frequently linked to a more aggressive phenotype, a higher likelihood of metastasis, and therapeutic resistance.[30] Tumors with similar size and morphology may have different levels of hypoxia and tumor vascularity. At the beginning of the study, before the treatment, all groups of rat breast tumor were confirmed to have equivalent hypoxic tumor volume and tumor vascularity (Figure 7). After the treatments, the hypoxic


https://doi.org/10.1021/acsami.3c03184
ACS Appl. Mater. Interfaces XXXX, XXX, XXX−XXX

**Table 3. Pharmacokinetic Parameters of PLB, Nontargeted NPs (PLB-CS-*g*-Egen NPs), and Targeted NPs (PLB-CS-*g*-Egen NPs) after Intravenous Injection at an Equivalent PLB Dose of 5.91 mg/kg[a]**

| parameters | PLB (mean ± SD[b]) | PLB-CS NPs (mean ± SD[b]) | PLB-CS-*g*-Egen NPs (mean ± SD[b]) |
|---|---|---|---|
| $AUC_{total}$ (ng·h/mL) | 18,382.37 ± 1265.76 | 47,201.11 ± 1345.32 | 53,196.62 ± 1264.62 |
| $C_{max}$ (ng/mL) | 4948.94 ± 129.78 | 4808.03 ± 62.85 | 5186.33 ± 48.34 |
| $T_{1/2}$ (h) | 17.31 ± 0.62 | 32.90 ± 5.89 | 33.45 ± 6.05 |
| MRT (h) | 15.06 ± 0.35 | 39.16 ± 9.35 | 39.96 ± 4.87 |
| $V_d$ (L/kg) | 1.45 ± 0.03 | 0.83 ± 0.04 | 0.74 ± 0.03 |
| $Cl_{total}$ (mL/kg·h) | 57.92 ± 0.52 | 17.47 ± 0.95 | 15.39 ± 0.82 |
| $K_E$ ($h^{-1}$) | 0.040 ± 0.001 | 0.021 ± 0.004 | 0.020 ± 0.002 |
| $F_R$ | | 2.57 | 2.89 |

[a]Blank CS NPs: blank chitosan nanoparticles; PLB-CS NPs: nontargeted PLB loaded chitosan nanoparticles; and PLB-CS-Egen NPs: estrogen receptor targeted PLB loaded chitosan nanoparticles. [b]$n$ = 3; SD: standard deviation

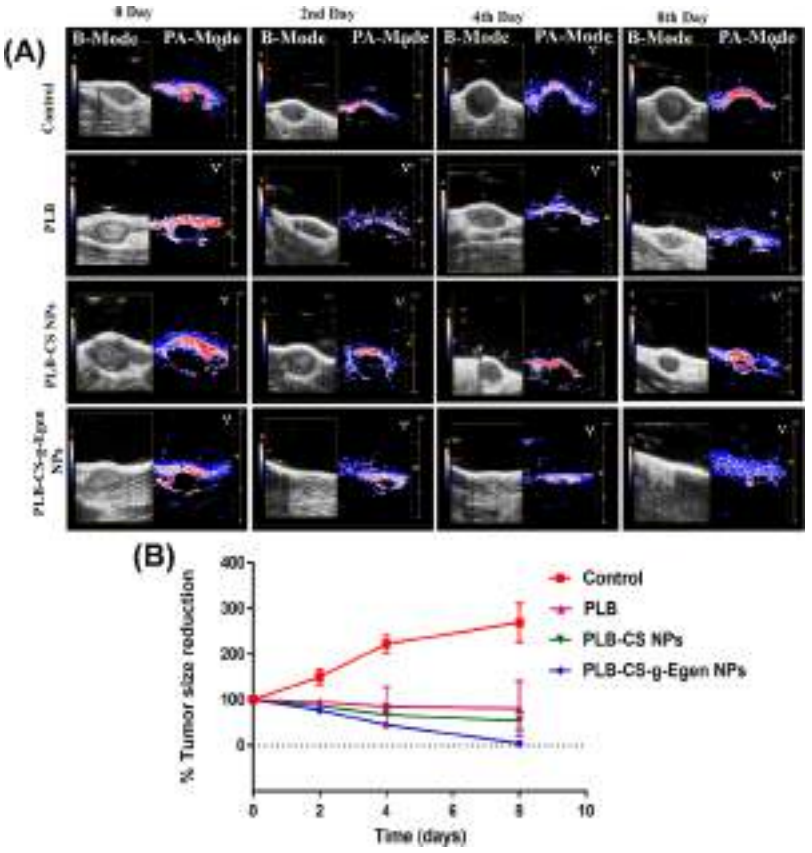


**Figure 6.** (A) Ultrasound and photoacoustic imaging of the breast tumor before and after treatment with PLB, PLB-CS NPs, and PLB-CS-Egen NPs. (B) Effect of the treatment with PLB, PLB-CS NPs, and PLB-CS-Egen NPs on the tumor size in rats.

tumor volume was significantly reduced in the NP treatment group ($p < 0.05$), and at the eighth day after the treatments with targeted NPs, hypoxic tumor volume completely vanished, but the free PLB treated and nontargeted NPs treated group showed hypoxic tumor volumes of 24.18 ± 2.13 and 17.45 ± 2.10 $mm^3$. In the case of the control group, the hypoxic tumor volume (116.53 ± 5.11 $mm^3$) was significantly increased ($p < 0.0001$) relative to its 0 day hypoxic tumor volume (29.94 ± 1.02 $mm^3$) (Figure 7A,B).

For the proliferation of the tumor, it requires a continuous supply of nutrients to the tumor cells in a higher amount that provokes the development of the blood vessels (angiogenesis) inside and outside of the tumor. After the treatment with targeted NPs, angiogenesis was stopped, was further reduced as the days progressed, and finally vanished at the eighth day of treatments in the animal group receiving the targeted treatments (Figure 8A,B). Meanwhile, the nontargeted NP treatment group had a slight reduction in the tumor vasculature up to the fourth day, but at the eighth day after the treatments, the tumor vasculature was significantly reduced. The free PLB treatment group also showed a slight reduction in the tumor vasculature. Further, the control group of rats showed an increase in the tumor vasculature at 2 days, a slight reduction at 4 days, and a further reduction at 8 days.

Additionally, after 8 days, the leftover tumors in these four groups of rats were extracted and subjected to H & E staining, and images were captured by using a light microscope (40×). Figure S8A demonstrates the normal breast stroma without any sign of the tumor (normal rats). In the treatment control (DMBA induced breast tumor) group receiving saline, the tumor has grown in the lobes of the breast with abnormal small and large nucleus/nuclei. Additionally, the DMBA treated rat


https://doi.org/10.1021/acsami.3c03184
ACS Appl. Mater. Interfaces XXXX, XXX, XXX−XXX

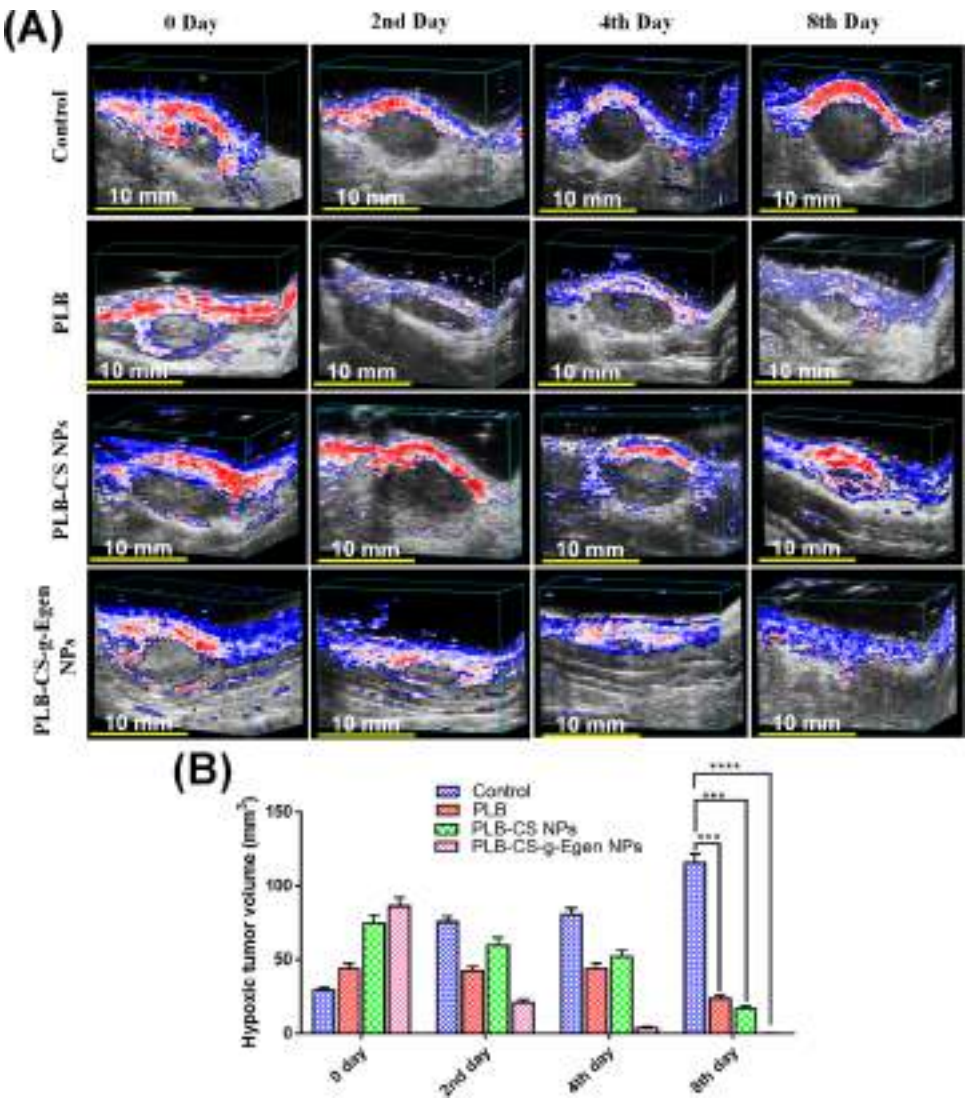


**Figure 7.** (A) Ultrasound and photoacoustic images of the breast tumor before and after treatment with PLB, PLB-CS NPs, and PLB-CS-Egen NPs and (B) analysis of the hypoxic tumor volume.

group's tumor was confirmed for ER expression by immunohistochemistry analysis; based on the ER scoring (College of American pathologist guidelines), 2% of the tumor cells exhibit nuclear staining (≥1% positive for ER). The obtained images were converted to black and white (B & W) images and counted for the number of nuclei present in each by using the ImageJ software (Figure S8B). The numbers of nuclei counted in the normal, saline-treated, PLB-treated, PLB-CS NP-treated, and PLB-CS-*g*-Egen NP-treated rat breast tumor samples were 80 ± 7.6, 968 ± 16.09, 851 ± 13.76, 580 ± 8.54, and 167 ± 4.18, respectively (Figure S8C). The separated nuclei of the animal groups treated with saline were 80 ± 7.6, which increased to 968 ± 16.09 ($p < 0.0001$) in the animals after DMBA treatment. The increase in nucleus area represents the establishment of breast tumor. After 8 days of treatment with free PLB, no significant effects on the tumor were observed, whereas nontargeted NPs ($p < 0.001$) showed a slight improvement and targeted NPs ($p < 0.0001$) demonstrated a significant reduction of the abnormal small and large nucleus/nuclei (Figure S8). Overall, targeted NPs are highly effective against DMBA induced breast cancer.

The survival study in the DMBA induced breast tumor rats post-treatment is presented in Figure S9. The study was conducted for 18 weeks, and Kaplan−Meier survival analysis was performed to calculate the mean survival rate of the rats. The tumor bearing control rats receiving saline survived up to 5 weeks, whereas the PLB-treated rats survived up to 9 weeks. In rats treated with nontargeted NPs, 66.67% of the population survived up to 16 weeks, and the remaining rat was able to survive beyond 18 weeks. Rats treated with targeted NPs survived beyond 18 weeks, and their survival was similar to that of healthy rats.

***In Vivo* Breast Tumor Targeting Efficiency by IVIS Live Imaging.** *In vivo* fluorescence imaging (Figure S10A) demonstrated that of free DiD (control) and DiD-CS NPs, DiD-CS-*g*-Egen NPs were distributed to different body parts within 2 h. After 2 h of the administration, targeted NPs started accumulating in the breast tumor, but free DiD and nontargeted NP fluorescent signals were significantly less at the site of the tumor. Further, after 6 h of administration, it was observed that targeted NPs completely accumulated to the tumor site, whereas free DiD and nontargeted NP signals were still less at the tumor site. Moreover, after 8 h, the


https://doi.org/10.1021/acsami.3c03184
ACS Appl. Mater. Interfaces XXXX, XXX, XXX−XXX

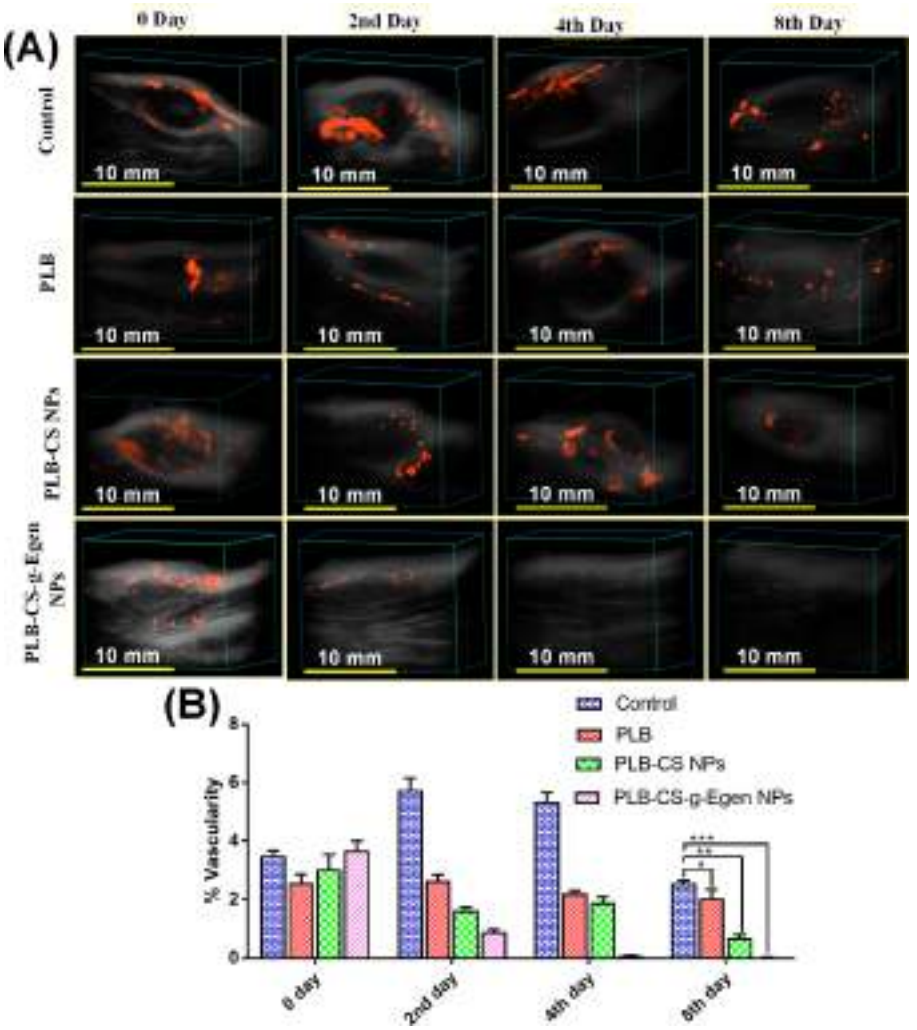


**Figure 8.** (A) Power Doppler images of the breast tumor before and after treatment with PLB, PLB-CS NPs, and PLB-CS-Egen NPs and (B) analysis of angiogenesis and tumor vascularity.

concentration of the targeted NPs started declining at the tumor site, which may be due to the metabolism or degradation of the NPs in the tumor microenvironment. Additionally, the image (Figure S10B) of the control rat (without DiD administration) does not show any fluorescent or background signal. The quantitative radiant efficiency signal from the free DiD, DiD-CS NPs, and DiD-CS-*g*-Egen NPs after administration is presented in Figure S10C. These results confirm the targeted delivery of CS-*g*-Egen NPs to breast tumors.

Recently, in a study, PLB loaded mesoporous silica NPs functionalized with MUC1 aptamer were prepared for targeted triple-negative breast cancer therapy. Additionally, indocyanine green loaded NPs were prepared for *in vivo* imaging of triple-negative breast cancer in Balb/c nude mice. The study demonstrated that MUC1 functionalized NPs selectively bind to the breast tumor. Hence, NPs conjugated with the targeting moiety can deliver the loaded drug to the targeted site for therapeutic applications.[75]

## CONCLUSIONS

In this research work, an Egen functionalized CS-based graft polymeric nano drug delivery system was developed for the targeted delivery of PLB to the ER-positive breast tumor. The entrapment efficiency of the PLB in the NPs was found to be up to 75.79%, which confirms that solvent evaporation followed by the ionic gelation method was suitable for the preparation of the NPs. The DLS, FE-SEM, TEM, and AFM analyses demonstrated that NPs were spherical in shape and had smooth surfaces. The presence of Egen on the outer surface of targeted NPs was confirmed by XPS analysis. The *in vitro* drug release study depicted that NPs were found to have sustained drug-releasing properties. The developed targeted NPs had more apoptosis-inducing properties compared with nontargeted NPs and free PLB, which were confirmed by the apoptosis study and cell cycle analysis. Targeted NPs were efficiently accumulated into the MCF7 cells as demonstrated in the cellular uptake study, and pretreatment of the cells with free Egen reduced the cellular uptake of the targeted NPs due to ER saturation, which confirms the receptor mediated endocytosis of the targeted NPs. The *in vitro* cytotoxicity assay in MCF7 cells and T47D cells suggested that targeted NPs were 57.34- and 30.32-fold more cytotoxic than the pure PLB, respectively. There was a 2−3-fold enhancement in the half-life and bioavailability of the NPs due to the entrapment of the PLB inside the NPs. The targeted NPs were capable of vanishing the DMBA induced breast tumor within 8 days of treatment, which was confirmed by ultrasound and photo-


https://doi.org/10.1021/acsami.3c03184
ACS Appl. Mater. Interfaces XXXX, XXX, XXX−XXX

acoustic imaging. Additionally, targeted NPs were capable of reducing the hypoxic tumor volume and tumor vascularity more efficiently compared with nontargeted and free PLB. Additionally, the biocompatibility and safety of the NPs were confirmed by an *in vitro* hemocompatibility and histopathology study. In summary, the developed targeted NPs showed great potential for delivering PLB to ERs-expressing hypoxic breast tumors.

## ■ ASSOCIATED CONTENT

### Supporting Information

The Supporting Information is available free of charge at https://pubs.acs.org/doi/10.1021/acsami.3c03184.

FTIR spectrum; $^1$H NMR spectrum; HRMS spectrum; particle size, zeta potential, and $T_{50}$ release graph; hemocompatibility study; cellular cytotoxicity assessment; apoptosis study; H & E staining of control and treated rats' breast tumor; Kaplan−Meier survival analysis; *in vivo* biodistribution of DiD, DiD-CS-NPs, and DiD-CS-*g*-Egen-NPs; and FTIR peak assignment (PDF)

## ■ AUTHOR INFORMATION


### Corresponding Author

**Madaswamy S. Muthu** − *Department of Pharmaceutical Engineering and Technology, Indian Institute of Technology, (BHU), Varanasi 221005 Uttar Pradesh, India;* orcid.org/0000-0001-5805-7921; Phone: +91 9235195928; Email: msmuthu. phe@itbhu.ac.in; Fax: +91 542 2368428

### Authors

**Abhishesh Kumar Mehata** − *Department of Pharmaceutical Engineering and Technology, Indian Institute of Technology, (BHU), Varanasi 221005 Uttar Pradesh, India*

**Virendra Singh** − *Cancer Biology Laboratory, Department of Zoology Institute of Science, (BHU), Varanasi 221005 Uttar Pradesh, India*

**Vikas** − *Department of Pharmaceutical Engineering and Technology, Indian Institute of Technology, (BHU), Varanasi 221005 Uttar Pradesh, India*

**Nitesh Singh** − *Department of Biochemistry, Institute of Medical Sciences, (BHU), Varanasi 221005 Uttar Pradesh, India*

**Abhijit Mandal** − *Department of Radiotherapy and Radiation Medicine, Institute of Medical Sciences, (BHU), Varanasi 221005 Uttar Pradesh, India*

**Debabrata Dash** − *Department of Biochemistry, Institute of Medical Sciences, (BHU), Varanasi 221005 Uttar Pradesh, India*

**Biplob Koch** − *Cancer Biology Laboratory, Department of Zoology Institute of Science, (BHU), Varanasi 221005 Uttar Pradesh, India;* orcid.org/0000-0001-9093-7793

Complete contact information is available at: https://pubs.acs.org/10.1021/acsami.3c03184


### Notes

The authors declare no competing financial interest.

## ■ ACKNOWLEDGMENTS

The authors acknowledge the support received as a teaching assistantship from the Ministry of Human Resource and Development (MHRD) and IIT BHU, Varanasi-221005. Additionally, we acknowledge SATHI-BHU for providing the ultrasound and photoacoustic imaging facility and CIF-IIT BHU for the instrumental characterization of nanoparticles.

## ■ REFERENCES


(1) Siegel, R. L.; Miller, K. D.; Jemal, A. Cancer Statistics, 2020. *Ca Cancer J. Clin.* **2020**, *70*, 7−30.

(2) Coles, C. E.; Anderson, B. O.; Cameron, D.; Cardoso, F.; Horton, R.; Knaul, F. M.; Mutebi, M.; Lee, N.; Abraham, J. E.; Anderson, B. O.; André, F.; Barrios, C. H.; Bliss, J. M.; Boughey, J. C.; Cameron, D. A.; Cardoso, F. V.; Carey, L. A.; Chatterjee, S.; Coles, C. E.; Cuzick, J.; du Plooy, D.; Francis, P. A.; Gralow, J. R.; Jagsi, R.; Knaul, F. M.; Ma, F.; Mann, R. M.; McIntosh, S. A.; Mertz, S. A.; Mutebi, M.; Olopade, F.; Phillips, K. A.; Poortmans, P. M.; Spanic, T.; Spence, D.; Stobart, H.; Symmans, F. W. F.; Villarreal-Garza, C.; Yip, C. H.; Bienz, M. J.; Drewett, L. M.; Fulton, A.; Inbah Rajah, D.; Kazmi, F.; Rubasingham, J.; Thompson, M.; Vargas, V.; Arreola, H.; Badwe, R. A.; Calderon Anyosa, R. J. C.; Dave, R. V.; de-Graft Aikins, A.; Earl, H. M.; Essue, B. M.; Etzioni, R. B.; Hawley, S. T.; Jiang, X.; Mittra, I.; Moreno, P. I.; Nargund, R. S.; Noble, C.; Smith, R. A.; Verhoeven, D.; Wang, J. N.; Watkins, D. A.; Zikmund-Fisher, B. J. The Lancet Breast Cancer Commission: Tackling A Global Health, Gender, and Equity Challenge. *Lancet* **2022**, *399*, 1101−1103.

(3) Mamnoon, B.; Feng, L.; Froberg, J.; Choi, Y.; Sathish, V.; Mallik, S. Hypoxia-Responsive, Polymeric Nanocarriers for Targeted Drug Delivery to Estrogen Receptor-Positive Breast Cancer Cell Spheroids. *Mol. Pharmaceutics* **2020**, *17*, 4312−4322.

(4) Nagini, S. Breast Cancer: Current Molecular Therapeutic Targets and New Players. *Anti-Cancer Agents Med. Chem.* **2017**, *17*, 152−163.

(5) Desantis, C. E.; Ma, J.; Gaudet, M. M.; Newman, L. A.; Miller, K. D.; Goding Sauer, A.; Jemal, A.; Siegel, R. L. Breast Cancer Statistics, 2019. *Ca. Cancer J. Clin.* **2019**, *69*, 438−451.

(6) Huang, B.; Omoto, Y.; Iwase, H.; Yamashita, H.; Toyama, T.; Coombes, R. C.; Filipovic, A.; Warner, M.; Gustafsson, J. Differential Expression of Estrogen Receptor A, B1, And B2 in Lobular and Ductal Breast Cancer. *Proc. Natl. Acad. Sci. U. S. A.* **2014**, *111*, 1933−1938.

(7) Maughan, K. L.; Lutterbie, M. A.; Ham, P. S. Treatment of Breast Cancer. *Am. Fam. Physician* **2010**, *81*, 1339−1346.

(8) Peart, O. Breast Intervention and Breast Cancer Treatment Options. *Radiol. Technol.* **2015**, *86*, 535m−558m. Quiz 559-562

(9) Kodali, A.; Gadi, V. K. Preoperative Systemic Therapy for Breast Cancer. *Surg. Clin. North. Am.* **2023**, *103*, 201−217.

(10) Burande, A. S.; Viswanadh, M. K.; Jha, A.; Mehata, A. K.; Shaik, A.; Agrawal, N.; Poddar, S.; Mahto, S. K.; Muthu, M. S. EGFR Targeted Paclitaxel and Piperine Co-Loaded Liposomes for The Treatment of Triple Negative Breast Cancer. *AAPS Pharmscitech.* **2020**, *21*, 151.

(11) Fisusi, F. A.; Akala, E. O. Drug Combinations in Breast Cancer Therapy. *Pharm. Nanotechnol.* **2019**, *7*, 3−23.

(12) Vikas; Sahu, H. K.; Mehata, A. K.; Viswanadh, M. K.; Priya, V.; Muthu, M. S. Dual-Receptor-Targeted Nanomedicines: Emerging Trends and Advances in Lung Cancer Therapeutics. *Nanomedicine* **2022**, *17*, 1375−1395.

(13) Xue, X.; Qu, H.; Li, Y. In Stimuli-Responsive Crosslinked Nanomedicine for Cancer Treatment. *Explor.* **2022**, *2*, 20210134.

(14) Zhang, X.; Niu, S.; Williams, G. R.; Wu, J.; Chen, X.; Zheng, H.; Zhu, L. M. Dual-Responsive Nanoparticles Based on Chitosan for Enhanced Breast Cancer Therapy. *Carbohydr. Polym.* **2019**, *221*, 84−93.

(15) Raveendran, R.; Chen, F.; Kent, B.; Stenzel, M. H. Estrone-Decorated Polyion Complex Micelles For Targeted Melittin Delivery To Hormone-Responsive Breast Cancer Cells. *Biomacromolecules* **2020**, *21*, 1222−1233.

(16) Kurmi, B. D.; Paliwal, R.; Paliwal, S. R. Dual Cancer Targeting Using Estrogen Functionalized Chitosan Nanoparticles Loaded With

Doxorubicin-Estrone Conjugate: A Quality by Design Approach. *Int. J. Biol. Macromol.* **2020**, *164*, 2881−2894.
(17) Tang, H.; Chen, J.; Wang, L.; Li, Q.; Yang, Y.; Lv, Z.; Bao, H.; Li, Y.; Luan, X.; Li, Y.; Ren, Z.; Zhou, X.; Cong, D.; Liu, Z.; Jia, J.; Chen, H.; Zhao, W.; Meng, Q.; Sun, F.; Pei, J. Co-Delivery of Epirubicin And Paclitaxel Using an Estrone-Targeted Pegylated Liposomal Nanoparticle for Breast Cancer. *Int. J. Pharm.* **2020**, *573*, No. 118806.
(18) Dhillon, S. Palbociclib: First Global Approval. *Drugs* **2015**, *75*, 543−551.
(19) Felip, E.; Llobera, L.; Perez-Mañá, C.; Quintela, D.; Guasch, I.; Margelí, M.; Teruel, I.; Cirauqui, B.; Centeno, C.; Romeo, M.; Ballana, E.; Quiroga, V.; Drugs, N. Old Toxicities: Pneumonitis Related to Palbociclib - A Case Report. *Breast Care* **2020**, *15*, 548−552.
(20) Farhat, F.; Tarabaih, M.; Kanj, A.; Aoun, M.; Kattan, J.; Assi, T.; Awada, A. Palbociclib Safety and Efficacy Beyond Ribociclib-Induced Liver Toxicity in Metastatic Hormone-Receptors Positive Breast Cancer Patient. *Anti-Cancer Drugs* **2020**, *31*, 85−89.
(21) Catlin, N. R.; Bowman, C. J.; Engel, S. M.; Sacaan, A.; Thibault, S.; Lewis, E. M.; Cappon, G. D. Reproductive and Developmental Toxicity Assessment of Palbociclib, A Cdk4/6 Inhibitor, In Sprague-Dawley Rats and New Zealand White Rabbits. *Reprod. Toxicol.* **2019**, *88*, 76−84.
(22) Kumar Mehata, A.; Bharti, S.; Singh, P.; Viswanadh, M. K.; Kumari, L.; Agrawal, P.; Singh, S.; Koch, B.; Muthu, M. S. Trastuzumab Decorated Tpgs-G-Chitosan Nanoparticles for Targeted Breast Cancer Therapy. *Colloids Surf., B* **2019**, *173*, 366−377.
(23) Muthu, M. S.; Kutty, R. V.; Luo, Z.; Xie, J.; Feng, S. S. Theranostic Vitamin E Tpgs Micelles of Transferrin Conjugation for Targeted Co-Delivery of Docetaxel and Ultra Bright Gold Nanoclusters. *Biomaterials* **2015**, *39*, 234−248.
(24) Fu, L.; Ma, X.; Liu, Y.; Xu, Z.; Sun, Z. Applying Nanotechnology to Boost Cancer Immunotherapy by Promoting Immunogenic Cell Death. *Chin. Chem. Lett.* **2022**, *33*, 1718−1728.
(25) Agarwal, S.; Sau, S.; Iyer, A. K.; Dixit, A.; Kashaw, S. K. Multiple Strategies For The Treatment Of Invasive Breast Carcinoma: A Comprehensive Prospective. *Drug Discovery Today* **2022**, *27*, 585−611.
(26) Mirza, Z.; Karim, S. Nanoparticles-Based Drug Delivery and Gene Therapy for Breast Cancer: Recent Advancements and Future Challenges. *Semin. Cancer Biol.* **2021**, *69*, 226−237.
(27) Kommineni, N.; Paul, D.; Saka, R.; Khan, W.; Nanjappan, S. Stealth Liposomal Chemotherapeutic Agent for Triple Negative Breast Cancer With Improved Pharmacokinetics. *NANO* **2022**, *6*, 424−435.
(28) Huang, Z.; Hu, H.; Xian, T.; Xu, Z.; Tang, D.; Wang, B.; Zhang, Y. Carrier-Free Nanomedicines Self-Assembled from Palbociclib Dimers and Ce6 for Enhanced Combined Chemo-Photodynamic Therapy of Breast Cancer. *RSC Adv.* **2023**, *13*, 1617−1626.
(29) Muz, B.; De La Puente, P.; Azab, F.; Azab, A. K. The Role of Hypoxia in Cancer Progression, Angiogenesis, Metastasis, and Resistance to Therapy. *Hypoxia* **2015**, *3*, 83−92.
(30) Zhang, Y.; Zhang, H.; Wang, M.; Schmid, T.; Xin, Z.; Kozhuharova, L.; Yu, W. K.; Huang, Y.; Cai, F.; Biskup, E. Hypoxia in Breast Cancer-Scientific Translation to Therapeutic and Diagnostic Clinical Applications. *Front. Oncol.* **2021**, *11*, No. 652266.
(31) Rockwell, S.; Dobrucki, I. T.; Kim, E. Y.; Marrison, S. T.; Vu, V. T. Hypoxia And Radiation Therapy: Past History, Ongoing Research, and Future Promise. *Curr. Mol. Med.* **2009**, *9*, 442−458.
(32) Liu, Q.; Palmgren, V. A. C.; Danen, E. H.; Le Dévédec, S. E. Acute Vs. Chronic Vs. Intermittent Hypoxia in Breast Cancer: A Review on Its Application in In Vitro Research. *Mol. Biol. Rep.* **2022**, *49*, 10961−10973.
(33) Sonali; Singh, R. P.; Sharma, G.; Kumari, L.; Koch, B.; Singh, S.; Bharti, S.; Rajinikanth, P. S.; Pandey, B. L.; Muthu, M. S. RGD-TPGS Decorated Theranostic Liposomes for Brain Targeted Delivery. *Colloids Surf., B* **2016**, *147*, 129−141.
(34) Xu, G.; Tang, H.; Chen, J.; Zhu, M.; Xie, Y.; Li, Y.; Hao, Q.; Sun, Y.; Cong, D.; Meng, Q.; Ren, Z.; Li, Q.; Bao, H.; Lv, Z.; Li, Y.; Pei, J. Estrone-Targeted Liposomes for Mitoxantrone Delivery Via Estrogen Receptor: In Vivo Targeting Efficacy, Antitumor Activity. *Eur. J. Pharm. Sci.* **2021**, *161*, No. 105780.
(35) Mehata, A. K.; Suseela, M. N. L.; Behera, C.; Kumari, P.; Mahto, S. K.; Muthu, M. S. Chitosan-Alginate Nanoparticles of Cabazitaxel: Design, Dual-Receptor Targeting and Efficacy in Lung Cancer Model. *Int. J. Biol. Macromol.* **2022**, *221*, 874−890.
(36) Esfandiarpour-Boroujeni, S.; Bagheri-Khoulenjani, S.; Mirzadeh, H. Modeling and Optimization of Degree of Folate Grafted on Chitosan and Carboxymethyl-Chitosan. *Prog. Biomater.* **2016**, *5*, 1−8.
(37) Viswanadh, M. K.; Vikas; Jha, A.; Reddy Adena, S. K.; Mehata, A. K.; Priya, V.; Neogi, K.; Poddar, S.; Mahto, S. K.; Muthu, M. S. Formulation and In Vivo Efficacy Study of Cetuximab Decorated Targeted Bioadhesive Nanomedicine for Non-Small-Cell Lung Cancer Therapy. *Nanomedicine* **2020**, *15*, 2345−2367.
(38) Mudigunda, S. V.; Pemmaraju, D. B.; Paradkar, S.; Puppala, E. R.; Gawali, B.; Upadhyayula, S. M.; Vegi Gangamodi, N.; Rengan, A. K. Multifunctional Polymeric Nanoparticles for Chemo/Photo-theranostics of Retinoblastoma. *ACS Biomater. Sci. Eng.* **2022**, *8*, 151−160.
(39) Agrawal, P.; Singh, R. P.; Kumari, L.; Sharma, G.; Koch, B.; Rajesh, C. V.; Mehata, A. K.; Singh, S.; Pandey, B. L.; Muthu, M. S. Tpgs-Chitosan Cross-Linked Targeted Nanoparticles for Effective Brain Cancer Therapy. *Mater. Sci. Eng.* **2017**, *74*, 167−176.
(40) Agrawal, P.; Singh, R. P.; Sharma, G.; Mehata, A. K.; Singh, S.; Rajesh, C. V.; Pandey, B. L.; Koch, B.; Muthu, M. S. Bioadhesive Micelles of D-A-Tocopherol Polyethylene Glycol Succinate 1000: Synergism of Chitosan and Transferrin in Targeted Drug Delivery. *Colloids Surf., B* **2017**, *152*, 277−288.
(41) Viswanadh, M. K.; Mehata, A. K.; Sharma, V.; Priya, V.; Varshney, N.; Mahto, S. K.; Muthu, M. S. Bioadhesive Chitosan Nanoparticles: Dual Targeting and Pharmacokinetic Aspects for Advanced Lung Cancer Treatment. *Carbohydr. Polym.* **2021**, *274*, No. 118617.
(42) Yilmaz, B.; Kadioglu, Y. Determination Of 17 B-Estradiol in Pharmaceutical Preparation By Uv Spectrophotometry and High Performance Liquid Chromatography Methods. *Arab. J. Chem.* **2017**, *10*, S1422−S1428.
(43) Jha, A.; Viswanadh, M. K.; Burande, A. S.; Mehata, A. K.; Poddar, S.; Yadav, K.; Mahto, S. K.; Parmar, A. S.; Muthu, M. S. Dna Biodots Based Targeted Theranostic Nanomedicine for The Imaging and Treatment of Non-Small Cell Lung Cancer. *Int. J. Biol. Macromol.* **2020**, *150*, 413−425.
(44) International, A, Standard Test Method for Analysis of Hemolytic Properties of Nanoparticles. Astm International West Conshohocken, Pa: 2013.
(45) Muthu, M. S.; Kulkarni, S. A.; Raju, A.; Feng, S. S. Theranostic Liposomes of Tpgs Coating for Targeted Co-Delivery of Docetaxel and Quantum Dots. *Biomaterials* **2012**, *33*, 3494−3501.
(46) Singh, R. P.; Sharma, G.; Singh, S.; Kumar, M.; Pandey, B. L.; Koch, B.; Muthu, M. S. Vitamin E Tpgs Conjugated Carbon Nanotubes Improved Efficacy of Docetaxel With Safety for Lung Cancer Treatment. *Colloids Surf., B* **2016**, *141*, 429−442.
(47) Turner, N. C.; Ro, J.; André, F.; Loi, S.; Verma, S.; Iwata, H.; Harbeck, N.; Loibl, S.; Huang Bartlett, C.; Zhang, K.; Giorgetti, C.; Randolph, S.; Koehler, M.; Cristofanilli, M. Palbociclib in Hormone-Receptor-Positive Advanced Breast Cancer. *N. Engl. J. Med.* **2015**, *373*, 209−219.
(48) Fischer, A. H.; Jacobson, K. A.; Rose, J.; Zeller, R. Hematoxylin and Eosin Staining of Tissue and Cell Sections. *Cold spring harbor protoc.* **2008**, *2008*, Pdb.Prot4986.
(49) Miller, J. L.; Bartlett, A. P.; Harman, R. M.; Majhi, P. D.; Jerry, D. J.; Van De Walle, G. R. Induced Mammary Cancer in Rat Models: Pathogenesis, Genetics, and Relevance to Female Breast Cancer. *J. Mammary Gland Biol. Neoplasia.* **2022**, *27*, 185−210.


https://doi.org/10.1021/acsami.3c03184
ACS Appl. Mater. Interfaces XXXX, XXX, XXX−XXX

(50) Larsen, M. C.; Angus, W. G.; Brake, P. B.; Eltom, S. E.; Sukow, K. A.; Jefcoate, C. R. Characterization of Cyp1b1 And Cyp1a1 Expression in Human Mammary Epithelial Cells: Role of The Aryl Hydrocarbon Receptor in Polycyclic Aromatic Hydrocarbon Metabolism. *Cancer Res.* **1998**, *58*, 2366−2374.
(51) Lin, Y.; Yao, Y.; Liu, S.; Wang, L.; Moorthy, B.; Xiong, D.; Cheng, T.; Ding, X.; Gu, J. Role of Mammary Epithelial and Stromal P450 Enzymes in The Clearance and Metabolic Activation of 7,12-Dimethylbenz(A)Anthracene in Mice. *Toxicol. Lett.* **2012**, *212*, 97−105.
(52) Alvarado, A.; Lopes, A. C.; Faustino-Rocha, A. I.; Cabrita, A. M. S.; Ferreira, R.; Oliveira, P. A.; Colaço, B. Prognostic Factors in Mnu and Dmba-Induced Mammary Tumors in Female Rats. *Pathol. Res. Pract.* **2017**, *213*, 441−446.
(53) Chow, L. W.; Cheung, M. N.; Loo, W. T.; Guan, X. Y. A Rat Cell Line Derived from Dmba-Induced Mammary Carcinoma. *Life Sci.* **2003**, *73*, 27−40.
(54) Yi, M.; Huo, L.; Koenig, K. B.; Mittendorf, E. A.; Meric-Bernstam, F.; Kuerer, H. M.; Bedrosian, I.; Buzdar, A. U.; Symmans, W. F.; Crow, J. R.; Bender, M.; Shah, R. R.; Hortobagyi, G. N.; Hunt, K. K. Which Threshold for Er Positivity? A Retrospective Study Based on 9639 Patients. *Ann. Oncol.* **2014**, *25*, 1004−1011.
(55) Tang, W.; Yang, Z.; Wang, S.; Wang, Z.; Song, J.; Yu, G.; Fan, W.; Dai, Y.; Wang, J.; Shan, L.; Niu, G.; Fan, Q.; Chen, X. Organic Semiconducting Photoacoustic Nanodroplets for Laser-Activatable Ultrasound Imaging and Combinational Cancer Therapy. *ACS Nano* **2018**, *12*, 2610−2622.
(56) Hannah, A.; Luke, G.; Wilson, K.; Homan, K.; Emelianov, S. Indocyanine Green-Loaded Photoacoustic Nanodroplets: Dual Contrast Nanoconstructs for Enhanced Photoacoustic and Ultrasound Imaging. *ACS Nano* **2014**, *8*, 250−259.
(57) Ture, M.; Tokatli, F.; Kurt, I. Using Kaplan−Meier Analysis Together With Decision Tree Methods (C&Rt, Chaid, Quest, C4. 5 And Id3) in Determining Recurrence-Free Survival of Breast Cancer Patients. *Expert Syst. Appl.* **2009**, *36*, 2017−2026.
(58) Ekinci, M.; Koksal-Karayildirim, C.; Ilem-Ozdemir, D. Radiolabeled Methotrexate Loaded Chitosan Nanoparticles as Imaging Probe for Breast Cancer: Biodistribution in Tumor-Bearing Mice. *J. Drug Delivery Sci. Technol.* **2023**, *80*, No. 104146.
(59) Holder, C. F.; Schaak, R. E. Tutorial on Powder X-Ray Diffraction for Characterizing Nanoscale Materials. *ACS Nano* **2019**, *13*, 7359−7365.
(60) Zheng, S.; Peng, J.; Xu, K.; Tang, P. X.; Ma, X.; Huang, Y.; Chen, L.; Li, H. X-Ray Powder Diffraction Data for Palbociclib, C24h29n7o2. *Powder Diffr.* **2016**, *31*, 248−250.
(61) Toft, N. J.; Axelsen, T. V.; Pedersen, H. L.; Mele, M.; Burton, M.; Balling, E.; Johansen, T.; Thomassen, M.; Christiansen, P. M.; Boedtkjer, E. Acid-Base Transporters and Ph Dynamics in Human Breast Carcinomas Predict Proliferative Activity, Metastasis, And Survival. *Elife* **2021**, *10*, No. E68447.
(62) Lin, B.; Chen, H.; Liang, D.; Lin, W.; Qi, X.; Liu, H.; Deng, X. Acidic Ph And High-H(2)O(2) Dual Tumor Microenvironment-Responsive Nanocatalytic Graphene Oxide for Cancer Selective Therapy and Recognition. *ACS Appl. Mater. Interfaces* **2019**, *11*, 11157−11166.
(63) Herdiana, Y.; Wathoni, N.; Shamsuddin, S.; Muchtaridi, M. Drug Release Study of The Chitosan-Based Nanoparticles. *Heliyon* **2022**, *8*, No. e08674.
(64) Mills, J. A.; Liu, F.; Jarrett, T. R.; Fletcher, N. L.; Thurecht, K. J. Nanoparticle Based Medicines: Approaches for Evading and Manipulating The Mononuclear Phagocyte System and Potential for Clinical Translation. *Biomater. Sci.* **2022**, *10*, 3029−3053.
(65) Priya, V.; Vikas; Mehata, A. K.; Jain, D.; Singh, S. K.; Muthu, M. S. Efficient Delivery of Abciximab Using Mesoporous Silica Nanoparticles: In-Vitro Assessment for Targeted and Improved Antithrombotic Activity. *Colloids Surf., B* **2022**, *218*, No. 112697.
(66) Rajan, M.; Praphakar, R. A.; Govindaraj, D.; Arulselvan, P.; Kumar, S. S. Cytotoxicity Assessment of Palbociclib-Loaded Chitosan-Polypropylene Glycol Nano Vehicles for Cancer Chemotherapy. *Mater. Today Chem.* **2017**, *6*, 26−33.
(67) Parsian, M.; Mutlu, P.; Taghavi Pourianazar, N.; Yalcin Azarkan, S.; Gunduz, U. Investigation of The Therapeutic Effects of Palbociclib Conjugated Magnetic Nanoparticles on Different Types of Breast Cancer Cell Lines. *Cell Mol. Bioeng.* **2023**, *16*, 143−157.
(68) Zivadinovic, D.; Gametchu, B.; Watson, C. S. Membrane Estrogen Receptor-Alpha Levels in Mcf-7 Breast Cancer Cells Predict Camp and Proliferation Responses. *Breast Cancer Res.* **2005**, *7*, R101−R112.
(69) Zang, Y.; Odwin-Dacosta, S.; Yager, J. D. Effects of Cadmium on Estrogen Receptor Mediated Signaling and Estrogen Induced Dna Synthesis in T47D Human Breast Cancer Cells. *Toxicol. Lett.* **2009**, *184*, 134−138.
(70) Chen, W.; Zhang, W.; Chen, M.; Yang, C.; Fang, T.; Wang, H.; Reid, L. M.; He, Z. Applications and Mechanisms of The Cyclin-Dependent Kinase 4/6 Inhibitor, Pd-0332991, in Solid Tumors. *Cell Oncol.* **2022**, *45*, 1053−1071.
(71) Cao, H.; Li, C.; Qi, W.; Meng, X.; Tian, R.; Qi, Y.; Yang, W.; Li, J. Synthesis, Cytotoxicity and Antitumour Mechanism Investigations of Polyoxometalate Doped Silica Nanospheres on Breast Cancer MCF-7 Cells. *PLoS One* **2017**, *12*, No. E0181018.
(72) Vaupel, P.; Mayer, A. Hypoxia in Tumors: Pathogenesis-Related Classification, Characterization of Hypoxia Subtypes, and Associated Biological and Clinical Implications. *Adv. Exp. Med. Biol.* **2014**, *812*, 19−24.
(73) Hill, R. P.; Bristow, R. G.; Fyles, A.; Koritzinsky, M.; Milosevic, M.; Wouters, B. G. Hypoxia and Predicting Radiation Response. *Semin. Radiat. Oncol.* **2015**, *25*, 260−272.
(74) Brizel, D. M.; Scully, S. P.; Harrelson, J. M.; Layfield, L. J.; Bean, J. M.; Prosnitz, L. R.; Dewhirst, M. W. Tumor Oxygenation Predicts for The Likelihood of Distant Metastases in Human Soft Tissue Sarcoma. *Cancer Res.* **1996**, *56*, 941−943.
(75) Estepa-Fernández, A.; García-Fernández, A.; Lérida-Viso, A.; Morellá-Aucejo, Á.; Esteve-Moreno, J. J.; Blandez, J. F.; Alfonso, M.; Candela-Noguera, V.; Vivo-Llorca, G.; Sancenon-Galarza, F.; Orzáez, M.; Martínez-Máñez, R. Engineering Nanoparticle Communication in Living Systems by Stigmergy: An Application to Enhance Antitumor Therapy in Triple-Negative Breast Cancer. *Nano Today* **2023**, *48*, No. 101692.


https://doi.org/10.1021/acsami.3c03184
ACS Appl. Mater. Interfaces XXXX, XXX, XXX−XXX